Received: 16 November 2021 | Revised: 31 December 2021 | Accepted: 3 February 2022

DOI: 10.1002/gj.4419

RESEARCH ARTICLE

WILEY

Source rock evaluation within a sequence stratigraphic framework of the Palaeogene Liushagang Formation in the Fushan Depression, South China Sea

Bang Zeng[1] | Meijun Li[1,2] | Xin Wang[1] | Fangzheng Wang[1] | Chenglin Gong[1] | Jin Lai[1] | Yang Shi[3]

[1]State Key Laboratory of Petroleum Resources and Prospecting, College of Geosciences, China University of Petroleum (Beijing), Beijing, China

[2]Key Laboratory of Exploration Technologies for Oil and Gas Resources, Ministry of Education, College of Resources and Environment, Yangtze University, Wuhan, China

[3]Southern Oil Exploration and Development Company, PetroChina, Haikou, China

Correspondence
Meijun Li, State Key Laboratory of Petroleum Resources and Prospecting, College of Geosciences, China University of Petroleum (Beijing), Beijing, China.
Email: meijunli@cup.edu.cn, meijunli2008@hotmail.com

Funding information
Hainan Fushan Oilfield Exploration and Development Company, Grant/Award Number: 2020-HNYJ-003

Handling Editor: Z.-Q. Chen

The Fushan Depression is one of the prolific hydrocarbon-bearing depressions in the Beibuwan Basin, South China Sea. In this study, a total of 133 mudstone samples, 18 well-logging curves, and 12 seismic sections were analysed to investigate the geochemical features and spatial distribution of effective source rocks of the Palaeogene Liushagang Formation within a sequence stratigraphic geochemical framework. The results suggest that depositional centres of mudstones northward migrated from the central Huangtong Sag during the Liushagang period. Good hydrocarbon generation potential source rocks containing Type II kerogen occur in the transgressive systems tract (TST)–highstand systems tract (HST) of lower Liushagang sequence (SQls3), the middle Liushagang sequence (SQls2), and the lowstand systems tract (LST)–TST of upper Liushagang sequence (SQls1). The occurrence of effective source rock kitchens, which are mainly controlled by the thermal maturity is distributed in the strip-shaped area of SQls3 sequence, the whole Huangtong Sag of SQls2 sequence, and the central and northern part of Huangtong Sag of SQls1 sequence, respectively. Fewer hydrocarbon accumulations were found in the southern slope due to the relatively deeper hydrocarbon generation threshold depth and to the limited occurrence of effective source rock kitchens.

KEYWORDS
effective source rock kitchen, geochemical characteristics, sequence stratigraphic framework, source rock evaluation

1 | INTRODUCTION

Assessment of the hydrocarbon generation potential of source rocks is one of the key aspects of petroleum exploration and development (Magoon & Dow, 1994). Conventional source rock assessment mainly involves the determination of its amount of organic matter, the type of kerogen, and the level of maturation (He et al., 2019; Hunt, 1996; Peters, 1986; Sheikh, Faris, Shaker, & Kumral, 2016; Tissot & Welte, 1984). Most of these data are obtained by geochemical experiments in the laboratory. However, the measured data on the basis of drilling samples cannot reveal the sectional and areal heterogeneity due to the limitation of sample quantity and distribution.

Sequence stratigraphic methodology is a powerful tool for the description, interpretation, and nomenclature of sedimentary strata (Catuneanu, 2020). Due to its isochronism and extensionality, it greatly improves the scientificity and accuracy of reservoir prediction in petroleum exploration (Flint, Knight, & Tilbrook, 1998; Higgs et al., 2012; Kieft, Jackson, Hampson, & Larsen, 2010; Mancini, Obid, Badai, Liu, & Parcell, 2008). Recently, sequence stratigraphy combined with organic geochemical analysis has achieved good applications in source rock evaluation, oil-source correlation, and palaeoenvironmental evolution

studies (Lai, Li, Liu, Mao, Liu, et al., 2020; Lai, Li, Liu, Mao, Wang, et al., 2020; M. Li et al., 2018; Peters, Snedden, Sulaeman, Sarg, & Enrico, 2000; Souza et al., 2021; Xiao et al., 2019). The distribution and quality of source rocks have certain regularity within the sequence stratigraphic framework (Lai, Li, Liu, Mao, Liu, et al., 2020; Lai, Li, Liu, Mao, Wang, et al., 2020; M. Li et al., 2018).

The Fushan Depression is a Cenozoic petroleum-bearing tectonic unit in the Beibuwan Basin, South China Sea (Gan et al., 2020). After more than 60 years of exploration, numerous oil fields, such as Meitai, Huachang, Chaoyang, and Bailian oil fields, have been discovered successively (Lu et al., 2016). Much work has been done on source rocks. For example, the second member of the Palaeogene Liushagang Formation (Els_2) is the main source bed, and the eastern Bailian Sag and the western Huangtong Sag are the main petroleum-generating sags (Chen, Gan, Shi, Zhao, & Wang, 2015; Gan et al., 2020). However, the studies on conventional source rock evaluation limited by samples distribution are mainly focused on the eastern Bailian Sag, resulting in the lack of research on hydrocarbon generation potential and distribution of source rocks in the western Huangtong Sag.

In this study, a comprehensive source rock evaluation was carried out within a sequence stratigraphic framework of the Palaeogene Liushagang Formation in the western region of the Fushan Depression. The hydrocarbon generation potential and spatial distribution of source rocks were discussed on the basis of systematic geochemical analyses of 133 potential source rock samples, well-loggings, and seismic sections. Combined with the amount, type, maturity, and occurrence of organic matter, the effective source kitchens were determined. The main controlling factors and location of effective source rock kitchens are of great significance to the selection of petroleum exploration targets. This study proves that sequence stratigraphic geochemistry has a good application effect in the evaluation of source rocks in lacustrine basins.

2 | GEOLOGICAL BACKGROUND

The Fushan Depression is located in the south-east of the Beibuwan Basin (Figure 1a). It is a Cenozoic rift depression bounded to the north-west by the Lingao Fault, to the north-east by the Changliu

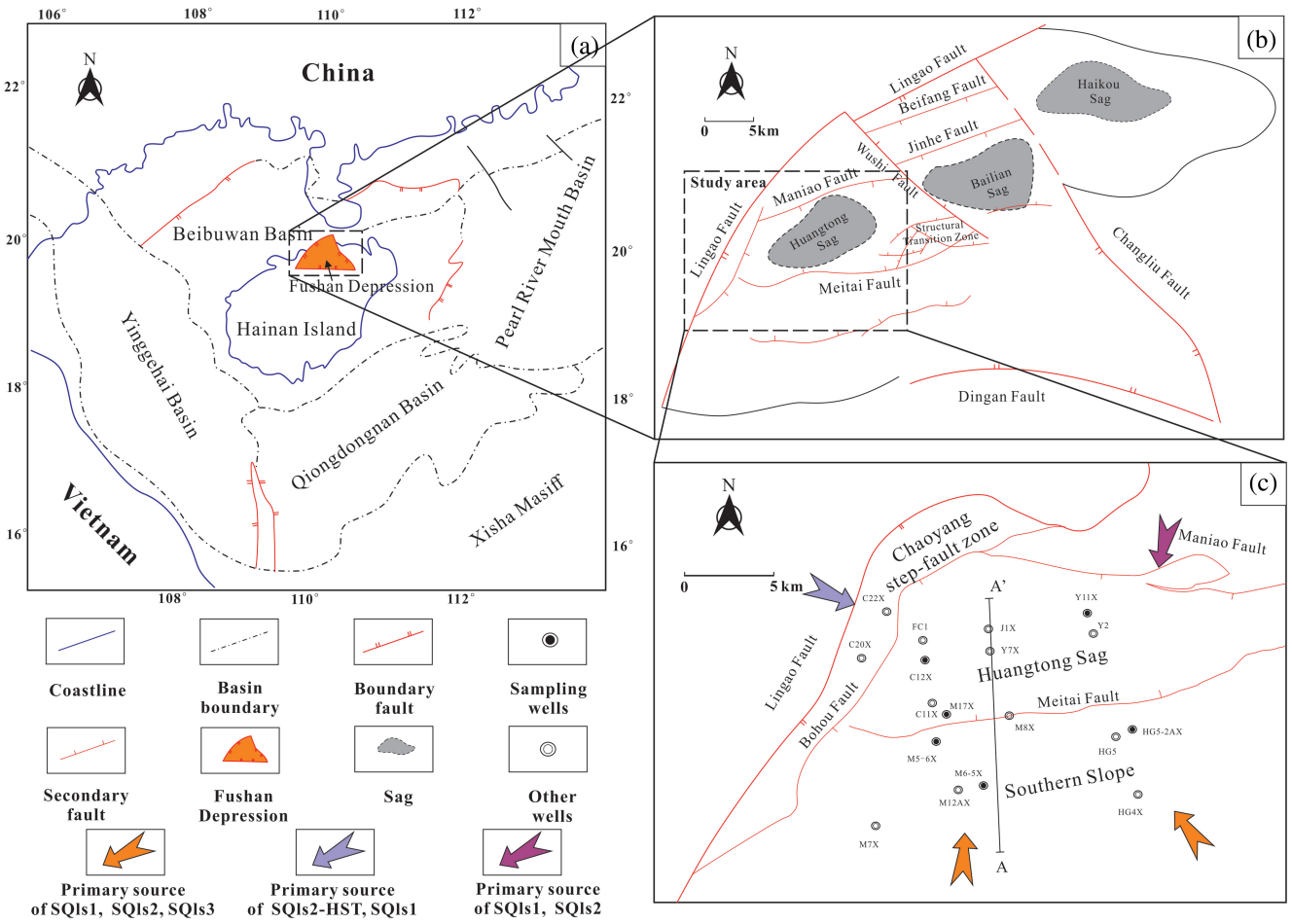

FIGURE 1 (a) Location of the Fushan Depression (modified after Liu et al., 2014). (b) Division of structural units in the Fushan Depression (modified after Gan et al., 2020). (c) The sketch map of the western region of Fushan Depression and wells location. Sediment source directions of the Liushagang depositional period are from Y. Li, Lin, Wang, & Luo, 2017

Fault, and to the south by the Ding'an Fault (Figure 1b). The Beibuwan Basin has experienced three stages of tectonic evolution: (a) an early extensional phase from Palaeocene to Eocene; (b) a late extensional phase of Oligocene age; and (c) a passive thermal subsidence phase from late Miocene to Recent (Gong, Li, & Xie, 1997; Liu et al., 2020). Separated by the structural transition zone, the Fushan Depression can be further divided into the Bailian Sag in the east and the Huangtong Sag in the west, which have different structural styles and depositional patterns (Liu, Wang, Lin, Li, & Ma, 2012). There are three Tertiary structural units in the west region from north to south (i.e., north Chaoyang step-fault zone, central Huangtong Sag, and south slope zone) (Liu et al., 2015). The southern slope area examined in this study covers approximately 8 km wide (Figure 1c).

The Palaeogene strata in the Fushan Depression consist of the Changliu Formation (Ech), the Liushagang Formation (Els), and the Weizhou Formation (Ewz) (Figure 2) (M. Li et al., 2008). The Liushagang Formation is the major oil-generating layer and reservoir and consists mainly of organic-rich mudstones, siltstones, and sandstones (Jin, Wang, Cao, Gan, & Chen, 2020). It can be divided into three third-order sequences (i.e., SQls3, SQls2, and SQls1) (Liu et al., 2014; Ma, Zhao, Liao, & Lin, 2012), which correspond to the first, second, and third members (Els_3, Els_2, and Els_1), respectively (Figure 2). The lake level and the activities of Meitai Fault, Bohou Fault, and Lingao Fault jointly control the sequence stratigraphic style, resulting in the absences of SQls2-LST–TST and SQls3 in the Huangtong Sag and SQls2-HST and SQls1 in the north-western side of the Bohou Fault (Figure 3).

During the depositional period of the Els, braided river delta systems were widely distributed in the southern slope, and fan delta systems were developed in the Chaoyang step-fault zone (Figure 3) (Y. Li et al., 2017; Liu et al., 2014, 2015, 2020). The central Huangtong Sag frosted turbidite fans and lacustrine facies with dark grey source rocks (Y. Li et al., 2017; Liu et al., 2014, 2015, 2020).

3 | MATERIALS AND METHODS

3.1 | Materials

A total of 133 core samples and cutting samples from the mudstone layers within the Liushagang Formation were collected for geochemical experiments. All the samples were designed for total organic

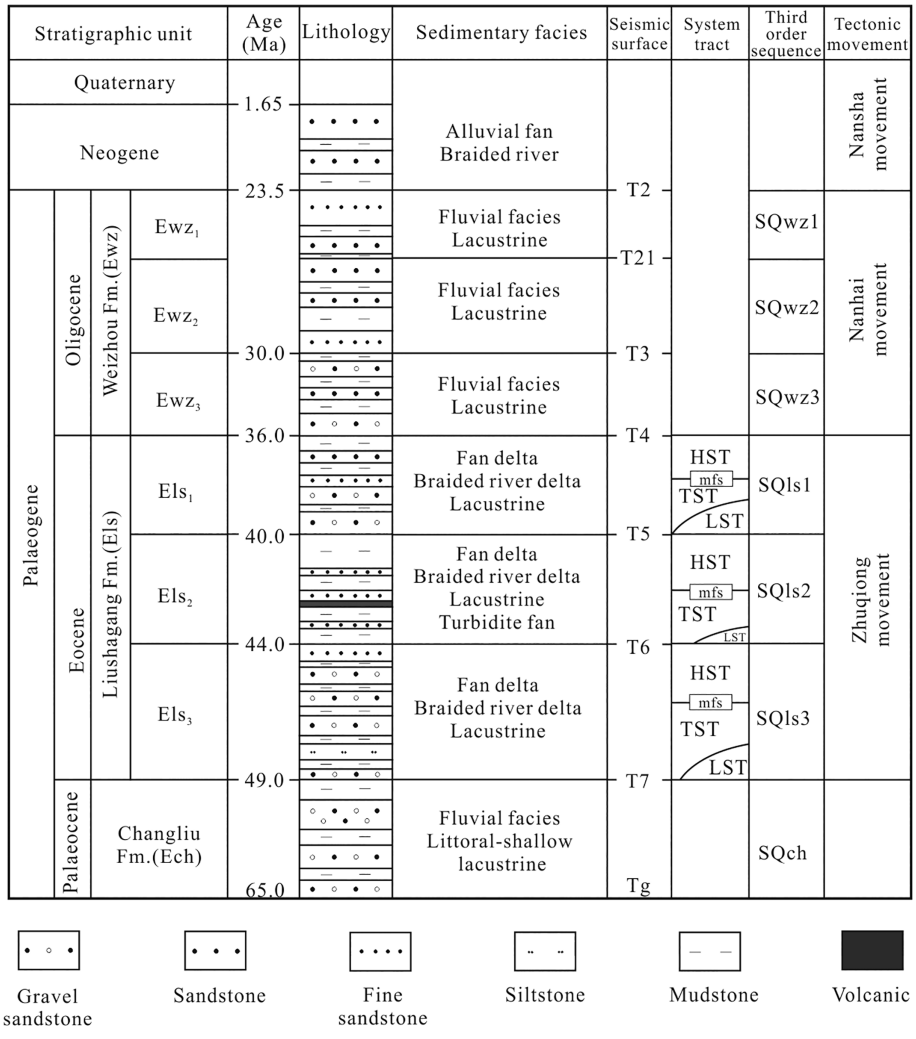

FIGURE 2 Generalized stratigraphic column and structural and stratigraphic sequence evolution of the Fushan Depression (modified after Liu et al., 2014). Els_N, the Nth member of the Liushagang Formation; Ewz_N, the Nth member of the Weizhou Formation

carbon (TOC) content analysis and Rock-eval pyrolysis. Twenty-eight samples were designed for vitrinite reflectance measurement. Eighteen well-logging curves and 12 seismic sections were collected for evaluation of the areal distribution of mudstones. In addition, the top and bottom depth contour maps of Els_3, Els_2, and Els_1 members were collected for the study of regional thermal maturity. The location of sampling wells and other wells are shown in Figure 1c.

3.2 | Geochemical experiments

At first, all the mudstone samples were rinsed with deionized water to remove residual contamination. Second, crushing and grinding them to less than 0.2 mm (80 mesh). The TOC content was measured using a LECO CS-230 carbon analyser after the carbonates were removed by dilute hydrochloric acid (1.5 mol/L). Rock-eval pyrolysis was carried

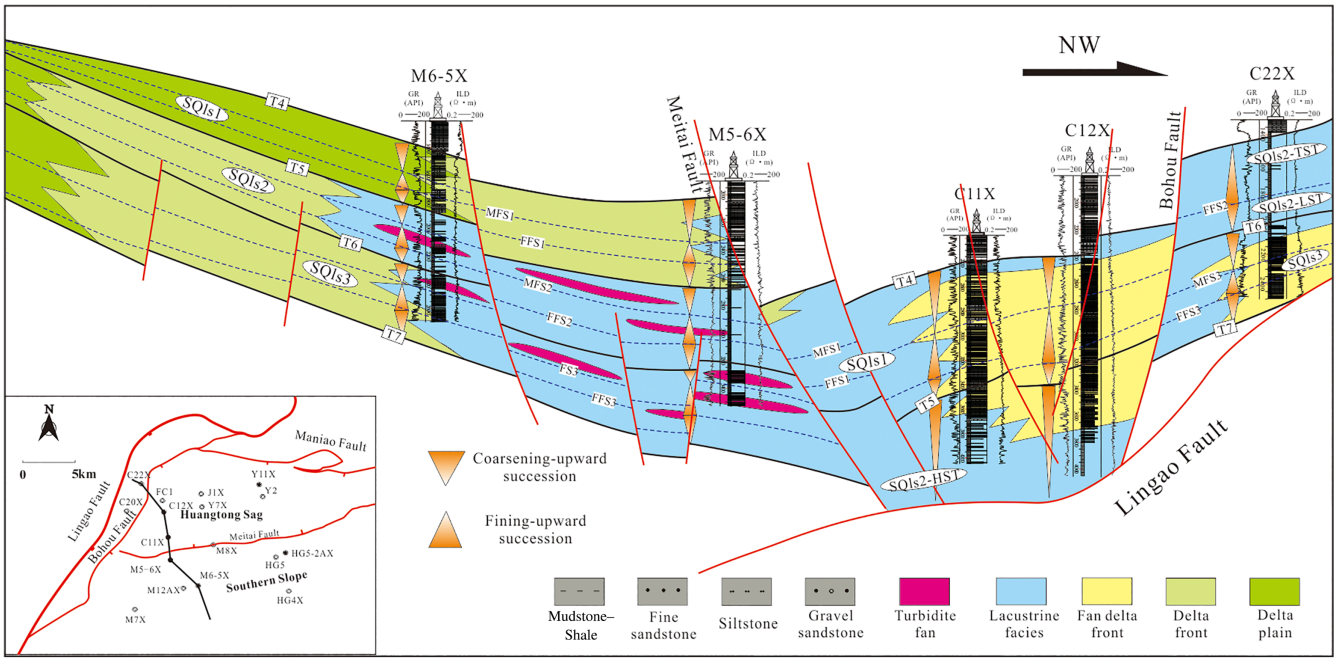

FIGURE 3 The depositional characteristics within the sequence stratigraphic of the western region of the Fushan Depression

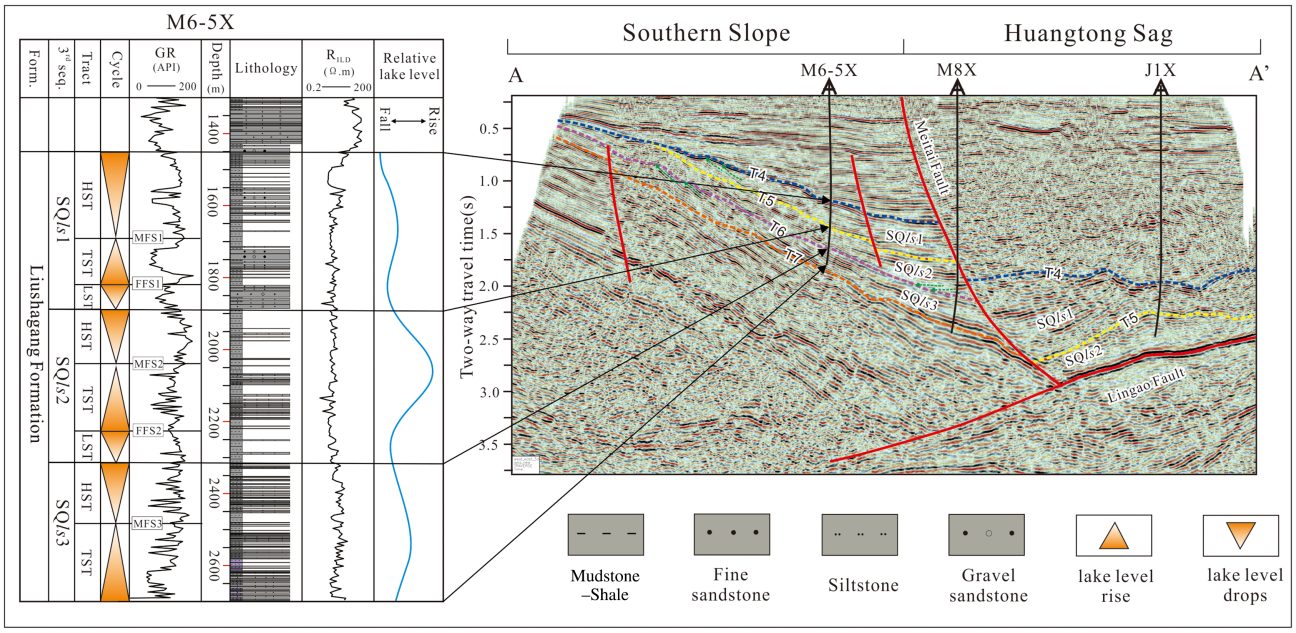

FIGURE 4 Sequence stratigraphic division of well M6-5X and representative seismic profile in the western region of the Fushan Depression. The position of the seismic profile can be seen in Figure 1. TST, transgressive systems tract; HST, highstand systems tract; LST, lowstand systems tract. Relative lake level is from Ma et al., 2012

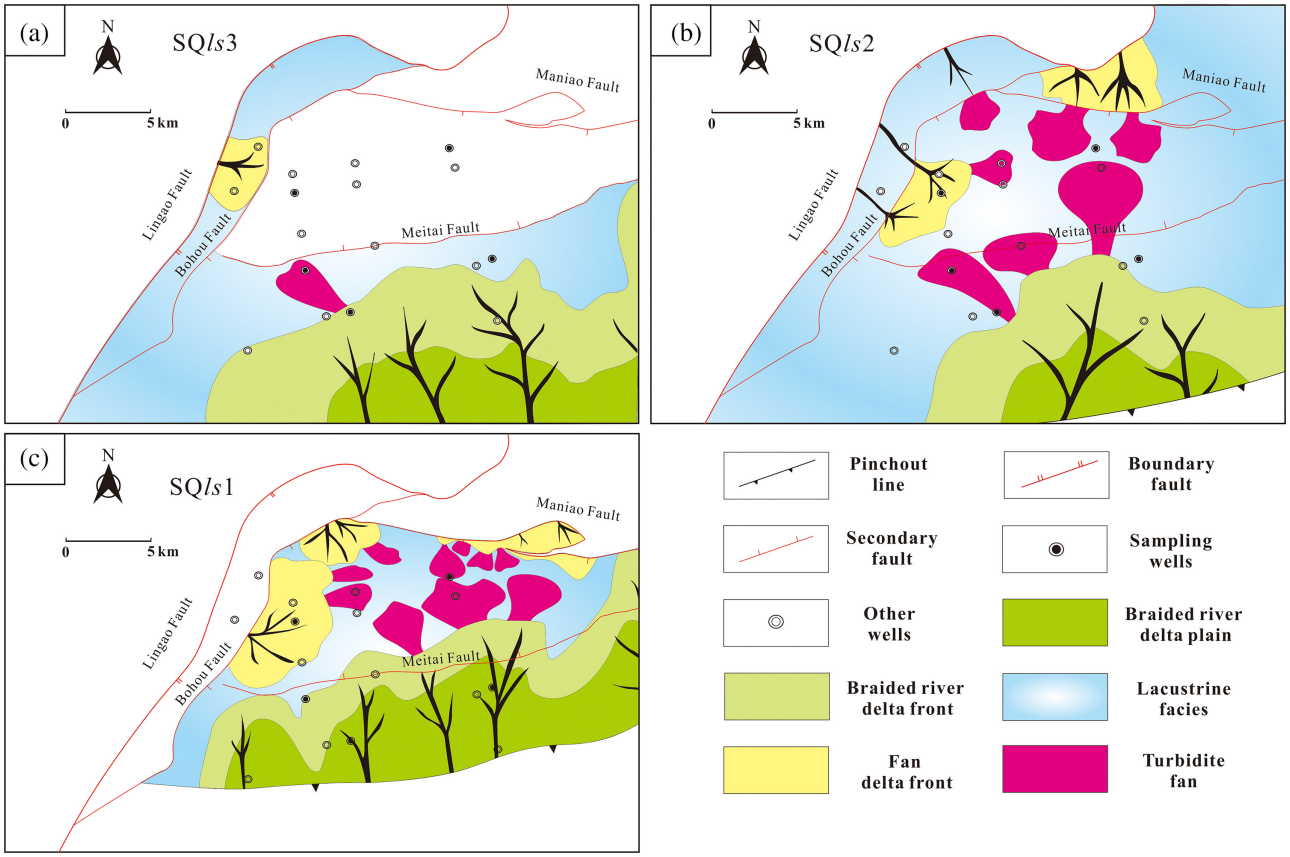

FIGURE 5 Planar depositional facies distribution of SQls3 (a), SQls2 (b), and SQls1 (c) of the Liushagang Formation in the western region of the Fushan Depression

out by OGE-VI Rock Pyrolysis Instrument. The ground samples weighing 100 mg were heated to 600°C to measure volatile hydrocarbon content (S_1), remaining hydrocarbon generation potential (S_2), and temperature corresponding to maximum pyrolysis yield (T_{max}). The vitrinite reflectance (*Ro*) measurements were performed on polished rock blocks using a Leica 6000-M microscope, adapted for reflected white light observation (M. Li, Simoneit, Zhong, & Fang, 2013; Rospondek, Szczerba, Malek, Góra, & Marynowski, 2008). Approximately 50 vitrinite grains were measured for each sample.

3.3 | Evaluation of mudstone areal distribution

The mudstone to stratum thickness ratio is an effective material to evaluate the areal distribution of mudstone (Lai, Li, Liu, Mao, Liu, et al., 2020). Y. Li et al. (2017) analysed the depositional setting of the Liushagang Formation, using three-dimensional seismic data. In this study, we first recognized the sedimentary facies of different sequences on the basis of previous studies and wells-correlation geological profiles. Then, the mudstone to stratum thickness ratios of different sedimentary facies was estimated based on logging curves and lithological logging data. After that, we established the corresponding relationship between logging and seismic data by well-seismic calibration and predicted the areal distribution of stratum thickness. Finally, the mudstone areal distribution was obtained by the comprehensive application of the mudstone to stratum thickness ratios, distribution of depositional facies, and calibrated thickness data.

4 | RESULTS

4.1 | Sequence stratigraphic and depositional characteristics

4.1.1 | Sequence stratigraphic framework

The Liushagang Formation was divided into three third-order sequences (SQls3, SQls2, and SQls1, from the bottom to top) by the T4, T5, T6, and T7 unconformities (Ma et al., 2012). In this study, we divided the sequences of each well based on the conventional logging and lithological logging data, and establish the correlation between the logging sequence interface and seismic sequence interface. Figure 4 shows the well M6-5X and corresponding seismic section, which were selected as the reference well and representative seismic section for the study of sequence stratigraphic framework.

The sequence boundaries are characterized by sharp changes in lithology with apparent correspondences of gamma ray (GR) and deep induction resistivity (R_{ILD}) on logging, and by the occurrence of

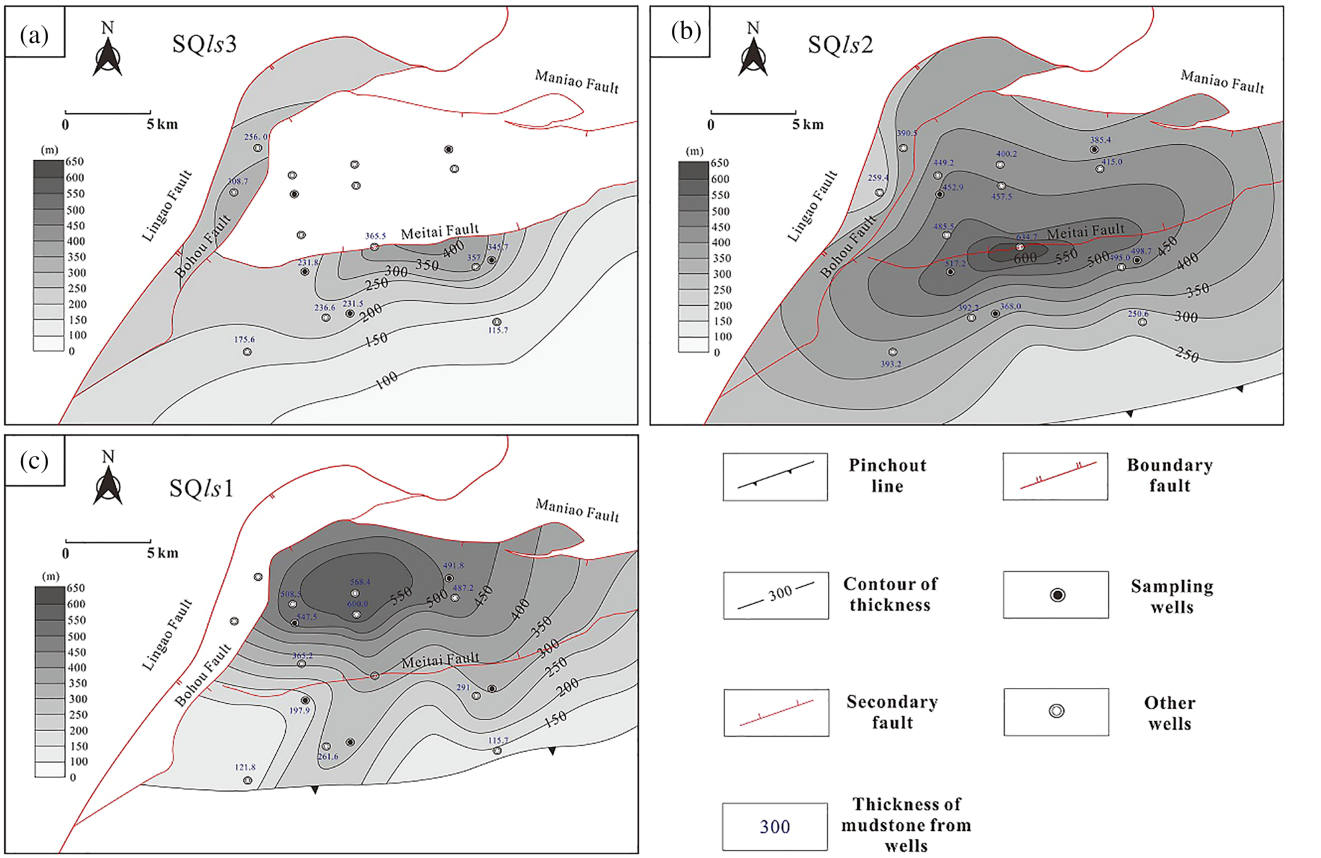

FIGURE 6 Areal distribution of mudstones of SQls3 (a), SQls2 (b), and SQls1 (c) of the Liushagang Formation in the western region of the Fushan Depression

seismically resolvable terminations of onlap, downlap, or truncation (Figure 4). Based on the retrogradational or progradational stacking patterns of parasequences, these third-order sequences of the Liushagang Formation can be further divided into nine system tracts (SQls3-LST, SQls3-TST, SQls3-HST, SQls2-LST, SQls2-TST, SQls2-HST, SQls1-LST, SQls1-TST, and SQls1-HST) (Figure 2). However, the bounding surfaces of these system tracts are, difficult to identify on seismic transects. The vertical stacking patterns of lithology and grain size are taken as the basis for elucidating the first flooding surfaces (FFS) and the maximum flooding surfaces (MFS) (Figure 4). Generally, the MFS and FFS are, respectively, characterized by the pure mudstone and by good correspondence with transformation interfaces of two parasequence sets characterized by weak progradational and evidently retrogradational stacking pattern.

4.1.2 | Depositional characteristics

Figure 3 shows the depositional characteristics and evolution within the Liushagang sequences of the western region of the Fushan Depression. Four main Depositional facies have been identified based on the lithology: braided river delta, semi-deep lake, fan delta, and turbidite fan. They are characterized by thick deltaic sandstones with minor interbedded mudstones, pure mudstones, multistage vertical superimposed gravel sandstones, and mudstones with sandstone and siltstone intervals, respectively.

During the deposition of SQls3, the lake level was relatively high (Figure 3). The sediments were transported to the deep lacustrine areas by the channel systems (Y. Li et al., 2017) (Figure 1c), and finally deposited as the braided river deltas, turbidite fans, and semi-deep lake facies in the western region of the Fushan Depression. The SQls2 was deposited during the highest lake level period of the Liushagang Formation (Figure 3), resulting in widespread distribution of dark mudstones. Southern uplift was the major provenance system (Figure 1c). Semi-deep lake facies were widely developed in the western region of the Fushan Depression. The lake level fell in the late HST period, and the western Lingao uplift provenance system began to transport sediments to the lacustrine (Figure 1c). As a result, fan delta facies were deposited in the west of Huangtong Sag. The SQls1 period with the lowest lake level (Figure 3). There are three provenance systems of the sediments: southern slope belt provenance system, western Lingao uplift provenance system, and north-eastern Maniao Fault provenance system, respectively (Y. Li et al., 2017) (Figure 1c). Braided river delta facies developed in the southern slope, fan delta facies deposited in the west and north-east of Huangtong Sag, and semi-deep lake facies distributed in the north of Huangtong Sag. The planar depositional facies distributions of different sequences are shown in Figure 5.

TABLE 1 Geochemical results of TOC, S_1, S_2, T_{max}, and *Ro* of the mudstone samples and their logging response characteristics

No.	Well	Sequence	Tract	Depth m	TOC %	S_1 mg/g	S_2 mg/g	T_{max} °C	S_1+S_2 mg/g	*Ro* %	AC μm/ft	GR API	RILD Ω·m	CNL %	DEN g/cm^3
1	HG5-2AX	SQls1	TST	1,717	1.56	0.53	5.64	418	6.17	–	111.54	150.10	2.93	50.27	2.25
2	HG5-2AX	SQls1	TST	1,739	0.95	0.18	2.09	437	2.27	–	107.64	157.48	2.71	47.28	2.26
3	HG5-2AX	SQls1	TST	1,779	1.07	0.19	2.65	440	2.84	0.42	111.94	152.92	1.92	40.24	2.27
4	HG5-2AX	SQls1	LST	1,908	0.83	0.12	1.67	435	1.79	–	98.73	96.89	2.16	26.11	2.19
5	HG5-2AX	SQls1	LST	1,952	0.95	0.22	1.88	436	2.1	0.44	102.67	161.02	1.85	34.27	2.30
6	HG5-2AX	SQls2	HST	2,097	1.30	0.22	3.43	434	3.65	0.51	93.95	174.59	3.06	47.43	2.41
7	HG5-2AX	SQls2	HST	2,120.5	1.51	0.31	4.05	435	4.36	–	106.87	189.41	2.50	44.89	2.28
8	HG5-2AX	SQls2	HST	2,141	1.55	0.41	4.3	435	4.71	–	92.85	178.36	3.56	35.35	2.52
9	HG5-2AX	SQls2	HST	2,175	1.53	0.29	4.38	434	4.67	–	93.20	152.93	3.44	37.90	2.43
10	HG5-2AX	SQls2	HST	2,204	2.14	0.14	5.57	433	5.71	–	90.92	126.20	2.45	28.17	2.28
11	HG5-2AX	SQls2	HST	2,253	1.68	0.41	4.83	434	5.24	–	102.92	195.76	4.06	55.25	2.43
12	HG5-2AX	SQls2	HST	2,350.5	1.57	0.45	4.1	439	4.55	0.53	107.24	191.12	2.66	49.34	2.12
13	HG5-2AX	SQls2	HST	2,422.5	1.93	0.73	5.08	438	5.81	–	83.87	198.72	7.10	39.83	2.24
14	HG5-2AX	SQls2	TST	2,450.5	1.99	0.32	5.06	438	5.38	–	82.80	169.63	5.30	36.78	2.36
15	HG5-2AX	SQls2	TST	2,494.5	2.04	0.27	5.09	438	5.36	–	95.27	165.26	4.18	46.04	2.07
16	HG5-2AX	SQls2	TST	2,571.5	2.01	0.24	5.14	437	5.38	–	93.68	172.76	4.18	47.11	2.31
17	HG5-2AX	SQls2	TST	2,633.5	2.00	0.37	5.15	437	5.52	0.54	91.09	187.10	3.72	42.70	2.44
18	HG5-2AX	SQls2	LST	2,671.5	1.99	0.36	4.85	438	5.21	–	85.14	159.34	5.56	38.62	2.48
19	HG5-2AX	SQls2	LST	2,765.5	1.66	0.17	4.27	440	4.44	–	83.78	188.89	6.53	44.25	2.44
20	HG5-2AX	SQls3	HST	2,856	1.59	0.5	4.14	438	4.64	0.54	85.57	157.50	5.71	29.92	2.27
21	HG5-2AX	SQls3	HST	2,909.5	1.80	0.4	3.53	432	3.93	–	77.42	164.66	13.65	20.28	2.55
22	HG5-2AX	SQls3	HST	2,936.5	1.83	0.45	4.09	438	4.54	–	88.28	184.80	7.04	24.48	2.50
23	HG5-2AX	SQls3	HST	2,978.5	1.50	0.27	3.19	438	3.46	–	79.35	188.58	6.96	26.21	2.48
24	HG5-2AX	SQls3	HST	3,020.5	1.46	0.32	3.42	440	3.74	–	75.87	157.46	10.00	26.39	2.68
25	HG5-2AX	SQls3	HST	3,073.5	1.65	0.53	4	436	4.53	–	64.12	179.52	8.70	18.75	2.60
26	HG5-2AX	SQls3	HST	3,117.5	1.47	0.17	3.39	436	3.56	–	64.07	177.53	9.34	15.06	2.62
27	HG5-2AX	SQls3	TST	3,156.5	2.09	0.24	4.7	443	4.94	–	85.21	171.49	6.66	43.53	2.42
28	HG5-2AX	SQls3	TST	3,193.5	2.19	0.49	5.53	444	6.02	0.57	82.64	186.02	9.78	32.57	2.54
29	HG5-2AX	SQls3	TST	3,241.5	1.66	0.19	3.67	442	3.86	–	69.30	178.44	8.98	24.68	2.51
30	HG5-2AX	SQls3	TST	3,311.5	1.76	0.38	4.56	438	4.94	–	79.04	192.04	5.62	30.55	2.58
31	HG5-2AX	SQls3	TST	3,368.5	1.84	0.29	4.02	441	4.31	0.63	80.70	169.88	7.69	26.52	2.57
32	M5-6X	SQls1	TST	2,451	1.44	0.31	4.12	437	4.43	0.48	75.15	142.82	6.38	53.57	2.26

(Continues)

TABLE 1 (Continued)

No.	Well	Sequence	Tract	Depth m	TOC %	S_1 mg/g	S_2 mg/g	T_{max} °C	S_1+S_2 mg/g	*Ro* %	AC μm/ft	GR API	RILD Ω·m	CNL %	DEN g/cm^3
33	M5-6X	SQIs1	LST	2,519	1.68	0.26	4.41	434	4.67	–	85.87	132.12	5.49	45.65	2.20
34	M5-6X	SQIs1	LST	2,624	2.82	0.3	6.33	436	6.63	0.51	75.73	146.76	14.10	47.82	2.51
35	M5-6X	SQIs2	HST	2,671	1.47	0.18	3.74	437	3.92	–	61.74	156.38	23.15	43.17	2.43
36	M5-6X	SQIs2	HST	2,693	1.79	0.14	4.4	437	4.54	–	73.82	147.31	10.31	52.89	2.33
37	M5-6X	SQIs2	HST	2,785	1.84	0.35	4.93	438	5.28	–	72.05	143.02	13.23	49.46	2.55
38	M5-6X	SQIs2	HST	2,834.5	1.70	0.19	4.56	440	4.75	–	74.09	159.41	10.71	40.48	2.35
39	M5-6X	SQIs2	TST	2,918.5	1.92	0.32	5.25	441	5.57	0.53	74.80	135.34	12.76	39.23	2.49
40	M5-6X	SQIs2	TST	3,009.5	1.68	0.24	3.72	440	3.96	–	80.35	147.82	6.53	37.85	2.34
41	M5-6X	SQIs2	LST	3,080.5	1.72	0.24	4.26	442	4.5	0.55	69.97	131.45	18.97	55.87	2.09
42	M5-6X	SQIs2	LST	3,147.5	1.77	0.42	4.87	446	5.29	–	65.51	141.60	28.89	56.01	2.52
43	M5-6X	SQIs3	HST	3,318.5	1.69	0.39	4.7	448	5.09	0.58	80.72	150.42	7.97	41.97	2.35
44	M5-6X	SQIs3	HST	3,331.5	1.61	0.3	4.31	444	4.61	–	80.62	141.11	9.43	36.90	2.59
45	M5-6X	SQIs3	TST	3,395.5	1.69	0.27	4.29	445	4.56	–	81.74	121.39	10.55	49.71	2.46
46	M5-6X	SQIs3	TST	3,506.5	1.13	0.21	2.54	445	2.75	0.61	76.09	146.87	8.77	48.26	2.28
47	M6-5X	SQIs1	HST	1,447	0.35	0.01	0.07	429	0.08	–	93.06	116.04	18.66	28.75	2.46
48	M6-5X	SQIs1	HST	1,483	0.57	0.04	0.28	420	0.32	–	93.58	141.70	4.40	39.96	2.27
49	M6-5X	SQIs1	HST	1,505	0.41	0.09	0.71	427	0.8	–	110.87	137.63	2.75	47.18	2.18
50	M6-5X	SQIs1	HST	1,533	1.08	0.25	3.04	434	3.29	–	102.95	138.37	2.19	49.60	2.20
51	M6-5X	SQIs1	HST	1,571.5	0.63	0.11	1.14	433	1.25	–	106.19	71.41	8.62	23.96	2.42
52	M6-5X	SQIs1	HST	1,599	0.75	0.19	1.87	435	2.06	–	97.74	131.96	5.99	31.94	2.19
53	M6-5X	SQIs1	HST	1,617	0.74	0.16	1.35	434	1.51	–	100.15	146.53	3.43	43.87	2.15
54	M6-5X	SQIs1	HST	1,643	1.11	0.37	2.68	435	3.05	–	101.64	140.86	3.75	39.75	2.29
55	M6-5X	SQIs1	HST	1,661	1.38	0.41	4.16	434	4.57	–	96.44	144.82	2.84	44.38	2.15
56	M6-5X	SQIs1	HST	1,711	1.02	0.09	2.29	432	2.38	–	112.38	131.12	3.09	40.35	2.39
57	M6-5X	SQIs1	TST	1,755	1.06	0.1	2.39	435	2.49	–	92.92	115.05	4.36	30.93	2.29
58	M6-5X	SQIs1	TST	1,805	1.32	0.27	3.46	432	3.73	–	99.39	134.84	4.25	40.89	2.31
59	M6-5X	SQIs1	LST	1,876	1.80	0.16	4.15	435	4.31	–	97.82	137.42	4.92	35.40	2.39
60	M6-5X	SQIs2	HST	1,890	1.67	0.16	3.87	434	4.03	–	101.96	150.08	2.76	47.41	2.40
61	M6-5X	SQIs2	HST	1,933	1.80	0.13	4.24	435	4.37	–	87.37	158.29	3.43	46.19	2.22
62	M6-5X	SQIs2	HST	1,975	1.75	0.12	3.87	435	3.99	–	99.60	164.99	4.34	52.96	2.31
63	M6-5X	SQIs2	HST	2,039	1.75	0.1	3.8	435	3.9	–	87.52	153.43	4.90	48.24	2.30
64	M6-5X	SQIs2	TST	2,077	1.90	0.13	4.67	434	4.8	–	85.17	136.20	4.41	28.54	2.46

TABLE 1 (Continued)

No.	Well	Sequence	Tract	Depth m	TOC %	S_1 mg/g	S_2 mg/g	T_{max} °C	S_1+S_2 mg/g	*Ro* %	AC μm/ft	GR API	RILD Ω·m	CNL %	DEN g/cm^3
65	M6-5X	SQIs2	TST	2,106.5	2.03	0.16	5.16	434	5.32	–	123.31	110.65	3.13	57.34	2.36
66	M6-5X	SQIs2	TST	2,145.5	2.18	0.18	6.11	435	6.29	–	78.07	137.27	3.45	36.20	2.49
67	M6-5X	SQIs2	TST	2,160	1.82	0.12	4.84	435	4.96	–	99.44	127.53	3.81	27.89	2.61
68	M6-5X	SQIs2	TST	2,185.5	1.90	0.11	4.46	436	4.57	–	78.72	144.47	5.07	37.61	2.30
69	M6-5X	SQIs2	LST	2,243.5	1.78	0.1	4.24	437	4.34	–	80.55	126.72	3.43	48.40	2.45
70	M6-5X	SQIs2	LST	2,256.5	1.69	0.06	3.26	438	3.32	–	78.17	144.52	4.52	40.32	2.45
71	M6-5X	SQIs2	LST	2,309	1.67	0.12	3.99	438	4.11	–	77.08	145.13	2.75	47.19	2.34
72	M6-5X	SQIs3	HST	2,345.5	1.60	0.07	3.27	437	3.34	–	70.01	153.46	4.68	52.29	2.55
73	M6-5X	SQIs3	HST	2,441.5	1.96	0.22	4.77	439	4.99	–	70.45	127.42	8.16	21.49	2.44
74	M6-5X	SQIs3	HST	2,468.5	2.17	0.29	6.98	440	7.27	–	76.95	154.13	3.78	43.71	2.17
75	M6-5X	SQIs3	HST	2,494.5	1.87	0.23	5.72	440	5.95	–	78.59	155.36	3.79	44.25	2.37
76	M6-5X	SQIs3	HST	2,514.5	1.83	0.21	5.26	439	5.47	–	74.93	163.97	6.89	40.09	2.27
77	M6-5X	SQIs3	TST	2,536.5	1.28	0.09	3.05	438	3.14	–	79.36	146.81	5.23	38.62	2.59
78	M6-5X	SQIs3	TST	2,575	1.32	0.12	3.37	440	3.49	–	106.03	142.02	12.39	25.65	2.50
79	C12X	SQIs1	HST	2,413.5	0.60	0.04	0.6	438	0.64	–	91.36	117.50	3.39	33.85	2.46
80	C12X	SQIs1	HST	2,465.5	0.75	0.03	1.06	438	1.09	–	90.95	130.49	3.06	40.72	2.53
81	C12X	SQIs1	HST	2,523.5	1.15	0.06	2.38	441	2.44	0.53	87.31	113.71	3.85	30.58	2.50
82	C12X	SQIs1	HST	2,689.5	1.18	0.1	2.62	441	2.72	–	90.58	130.50	3.45	38.13	2.47
83	C12X	SQIs1	HST	2,736	1.16	0.09	2.54	442	2.63	–	78.03	106.45	10.65	24.86	2.47
84	C12X	SQIs1	TST	2,813	1.26	0.18	3.08	442	3.26	–	76.81	96.92	7.95	15.94	2.47
85	C12X	SQIs1	TST	2,849	1.20	0.16	2.47	442	2.63	0.57	79.57	111.81	9.35	23.07	2.50
86	C12X	SQIs1	TST	2,901	1.43	0.19	3.34	440	3.53	–	78.89	86.01	10.74	13.98	2.45
87	C12X	SQIs1	TST	2,922.5	1.25	0.17	3.06	441	3.23	–	82.98	114.86	7.83	20.82	2.52
88	C12X	SQIs1	TST	3,026	1.70	0.23	4.47	442	4.7	0.61	79.69	120.09	9.56	24.71	2.52
89	C12X	SQIs1	TST	3,098.5	1.51	0.12	3.19	440	3.31	–	75.10	103.88	18.47	19.81	2.60
90	C12X	SQIs1	LST	3,153	1.91	0.31	4.64	442	4.95	–	76.41	112.95	11.81	24.72	2.60
91	C12X	SQIs1	LST	3,210	1.39	0.18	2.83	443	3.01	–	78.48	129.78	10.07	25.36	2.61
92	C12X	SQIs1	LST	3,220	1.18	0.14	2.43	443	2.57	–	77.82	97.58	17.44	16.13	2.56
93	C12X	SQIs1	LST	3,252.5	1.42	0.12	2.82	445	2.94	0.69	76.21	112.15	11.02	21.49	2.61
94	C12X	SQIs1	LST	3,274	1.71	0.07	1.68	444	1.75	–	77.22	128.59	12.75	25.37	2.61
95	C12X	SQIs1	LST	3,405	1.60	0.36	3.94	441	4.3	–	81.03	122.77	9.21	28.05	2.52
96	C12X	SQIs2	HST	3,448.5	1.94	0.3	5.11	446	5.41	–	81.25	133.14	10.58	24.37	2.52

(Continues)

TABLE 1 (Continued)

No.	Well	Sequence	Tract	Depth m	TOC %	S_1 mg/g	S_2 mg/g	T_{max} °C	S_1+S_2 mg/g	*Ro* %	AC μm/ft	GR API	RILD Ω·m	CNL %	DEN g/cm^3
97	C12X	SQIs2	HST	3,469	1.69	0.28	3.99	450	4.27	0.72	80.65	118.45	10.44	23.04	2.48
98	C12X	SQIs2	HST	3,521.5	1.79	0.36	4.72	449	5.08	0.78	78.71	131.34	13.05	23.84	2.59
99	C12X	SQIs2	HST	3,550	2.06	0.6	5.19	445	5.79	–	81.91	135.70	10.53	25.12	2.45
100	C12X	SQIs2	HST	3,608	1.87	0.3	4.05	445	4.35	–	79.31	151.44	11.66	29.04	2.50
101	C12X	SQIs2	HST	3,647.5	1.97	0.6	3.86	446	4.46	–	78.97	147.00	7.99	30.97	2.56
102	C12X	SQIs2	HST	3,690.5	1.43	0.3	3.29	447	3.59	–	71.51	158.03	18.54	25.41	2.57
103	C12X	SQIs2	HST	3,712.5	1.59	0.33	2.74	452	3.07	–	82.13	143.91	9.45	32.82	2.60
104	C12X	SQIs2	HST	3,756	1.64	0.31	2.79	450	3.1	0.92	83.70	156.87	9.40	31.06	2.57
105	C12X	SQIs2	HST	3,778.5	1.80	0.41	3.58	450	3.99	–	89.30	160.43	7.63	39.31	2.50
106	C12X	SQIs2	TST	3,806	1.75	0.56	4.12	449	4.68	–	88.05	164.48	6.53	40.58	2.53
107	C12X	SQIs2	TST	3,937.5	1.69	0.35	2.8	458	3.15	–	78.38	159.58	19.43	44.42	2.60
108	Y11X	SQIs1	HST	3,074.5	0.75	0.04	0.73	444	0.77	–	78.55	135.51	7.16	29.56	2.61
109	Y11X	SQIs1	HST	3,099.5	1.05	0.11	1.49	446	1.6	–	74.47	132.49	6.42	37.96	2.64
110	Y11X	SQIs1	HST	3,131.5	1.02	0.12	1.54	448	1.66	–	90.12	150.33	3.71	42.22	2.49
111	Y11X	SQIs1	HST	3,157	0.84	0.06	1.22	447	1.28	–	92.75	132.23	4.04	42.97	2.46
112	Y11X	SQIs1	HST	3,192	0.85	0.1	1.07	447	1.17	0.74	68.82	127.12	6.47	34.75	2.40
113	Y11X	SQIs1	HST	3,225.5	0.71	0.06	0.59	448	0.65	–	77.13	122.59	10.53	45.34	2.35
114	Y11X	SQIs1	HST	3,251.5	0.96	0.24	1.63	449	1.87	–	64.70	143.19	20.59	17.85	2.68
115	Y11X	SQIs1	HST	3,271.5	0.90	0.13	1.34	449	1.47	0.76	74.27	123.82	10.17	39.28	2.03
116	Y11X	SQIs1	HST	3,306.5	0.81	0.05	0.84	447	0.89	–	80.08	126.86	11.80	22.88	2.79
117	Y11X	SQIs1	HST	3,343.5	1.21	0.2	2.01	452	2.21	0.81	71.52	155.59	11.94	23.94	2.44
118	Y11X	SQIs1	TST	3,375.5	1.03	0.14	1.72	450	1.86	–	78.07	158.20	11.48	25.04	2.62
119	Y11X	SQIs1	TST	3,437	1.02	0.19	1.72	452	1.91	–	68.17	94.35	14.12	13.70	2.51
120	Y11X	SQIs1	TST	3,502.5	1.00	0.12	1.5	449	1.62	–	66.71	126.71	20.68	20.46	2.61
121	Y11X	SQIs1	TST	3,545.5	1.38	0.11	1.37	456	1.48	0.81	80.27	142.41	15.12	23.72	2.61
122	Y11X	SQIs1	TST	3,610	1.46	0.29	1.92	455	2.21	0.82	75.93	131.96	10.65	26.30	2.55
123	Y11X	SQIs1	TST	3,645.5	1.33	0.22	1.59	457	1.81	–	72.59	145.74	13.02	26.65	2.52
124	Y11X	SQIs1	LST	3,686.5	1.49	0.25	1.95	462	2.2	–	73.39	144.37	12.37	36.98	2.56
125	Y11X	SQIs1	LST	3,743.5	1.48	0.14	1.36	464	1.5	0.92	70.04	153.61	11.79	22.31	2.63
126	Y11X	SQIs1	LST	3,770	1.36	0.1	1.09	461	1.19	–	80.01	174.95	13.81	35.44	2.40
127	Y11X	SQIs1	LST	3,795.5	1.43	0.18	1.1	459	1.28	–	77.73	167.45	6.80	31.29	2.35

TABLE 1 (Continued)

No.	Well	Sequence	Tract	Depth m	TOC %	S_1 mg/g	S_2 mg/g	T_{max} °C	S_1+S_2 mg/g	Ro %	AC μm/ft	GR API	RILD Ω·m	CNL %	DEN g/cm^3
128	Y11X	SQls1	LST	3,815.5	1.29	0.18	1.02	468	1.2	–	75.85	151.42	11.26	22.76	2.69
129	Y11X	SQls1	LST	3,833	1.26	0.06	0.83	472	0.89	1.05	79.80	146.33	10.14	28.42	2.44
130	M17X	SQls3	LST	3,799.2	1.015	0.3	2.99	445	3.29	–	77.95	132.97	8.66	43.77	2.55
131	M17X	SQls3	LST	3,802	1.091	0.23	2.94	448	3.17	–	88.34	115.99	7.91	46.03	2.42
132	M17X	SQls3	LST	3,803.5	1.375	0.41	3.41	449	3.82	–	93.90	124.31	10.28	46.50	2.46
133	M17X	SQls3	LST	3,805	1.167	0.33	2.6	448	2.93	–	89.57	125.15	11.97	41.36	2.39

Note: Some TOC data of mudstone samples from well M5-6X and Y11X is cited from Zeng et al. (2021).

4.2 | Areal distribution of mudstones

For a lacustrine fluvial deltaic depositional system, the ranges of mudstone to stratum thickness ratio of deltaic, shallow lake, and deep lake facies are <0.5, 05–0.8, <0.8, respectively (Feng, 2004; Lai, Li, Liu, Mao, Liu, et al., 2020; Xie, Hu, Jia, & Hu, 2011). According to the lithological and logging data, we obtained the mudstone to stratum thickness ratio ranges of delta plains, delta fronts, fan delta fronts, turbidite fans, and semi-deep lake facies are <0.5, 0.6–0.8, 0.5–0.8, 0.6–0.8, >0.8, respectively. On the basis of mudstone to stratum thickness ratios, calibrated thickness data, and distribution of sedimentary facies, contour maps of mudstone thickness of the Liushang sequences were given in Figure 5. The thickness of SQls3 mudstone is between 100 and 400 m, and gradually decreases toward the south (Figure 6a). SQls2 mudstone thickness is about 250–600 m (Figure 6b). SQls3 mudstones with a thickness of about 150–550 m, and the thicker area is located in the northern part of Huangtong Sag (Figure 6c), which proves the northward migration of the lacustrine depositional centre.

4.3 | Geochemical analysis results

TOC, *R*o, and Rock-Eval pyrolysis data of the selected mudstone samples are shown in Table 1. The TOC values of samples are in the range of 0.35–2.82% (Only two samples have TOC content less than 0.5%), with an average of 1.47%, indicating that they meet the recognized source rock criterion (Peters, 1986; Peters & Cassa, 1994). Hydrocarbon generation potential index (GP = S_1 + S_2) was proposed by Tissot and Welte (1984) for source rock classification. The results of the Rock-Eval pyrolysis analysis show the values of GP ranging from 0.08 to 7.27 mg HC/g, indicating that poor to good source rocks occur in the Liushagang Formation. In addition, the T_{max} values and *R*o values vary from 418 to 472°C and 0.42 to 1.05%, respectively, indicating a thermal maturation level of immature to mature stage. Wide variation ranges of geochemical data demonstrate strong heterogeneity in the geochemical characteristics of source rocks of the Liushagang Formation.

5 | DISCUSSION

5.1 | TOC content estimation model

The average TOC data obtained from the laboratory measurement is used to represent the abundance of organic matter of the formation in traditional source rock evaluation. However, the results are limited by sample distribution and quantity, which makes it impossible to accurately characterize the spatial heterogeneity of geochemical characteristics (Lai, Li, Liu, Mao, Wang, et al., 2020). Therefore, conventional logging curves are used by petroleum geologists to estimate the TOC content of the formation due to its easy availability and vertical continuity (Fertl & Chilingar, 1988; Passey, Creaney, Kulla, Moretti, & Stroud, 1990; Schmoker, 1979). ΔlogR model is the most widely used

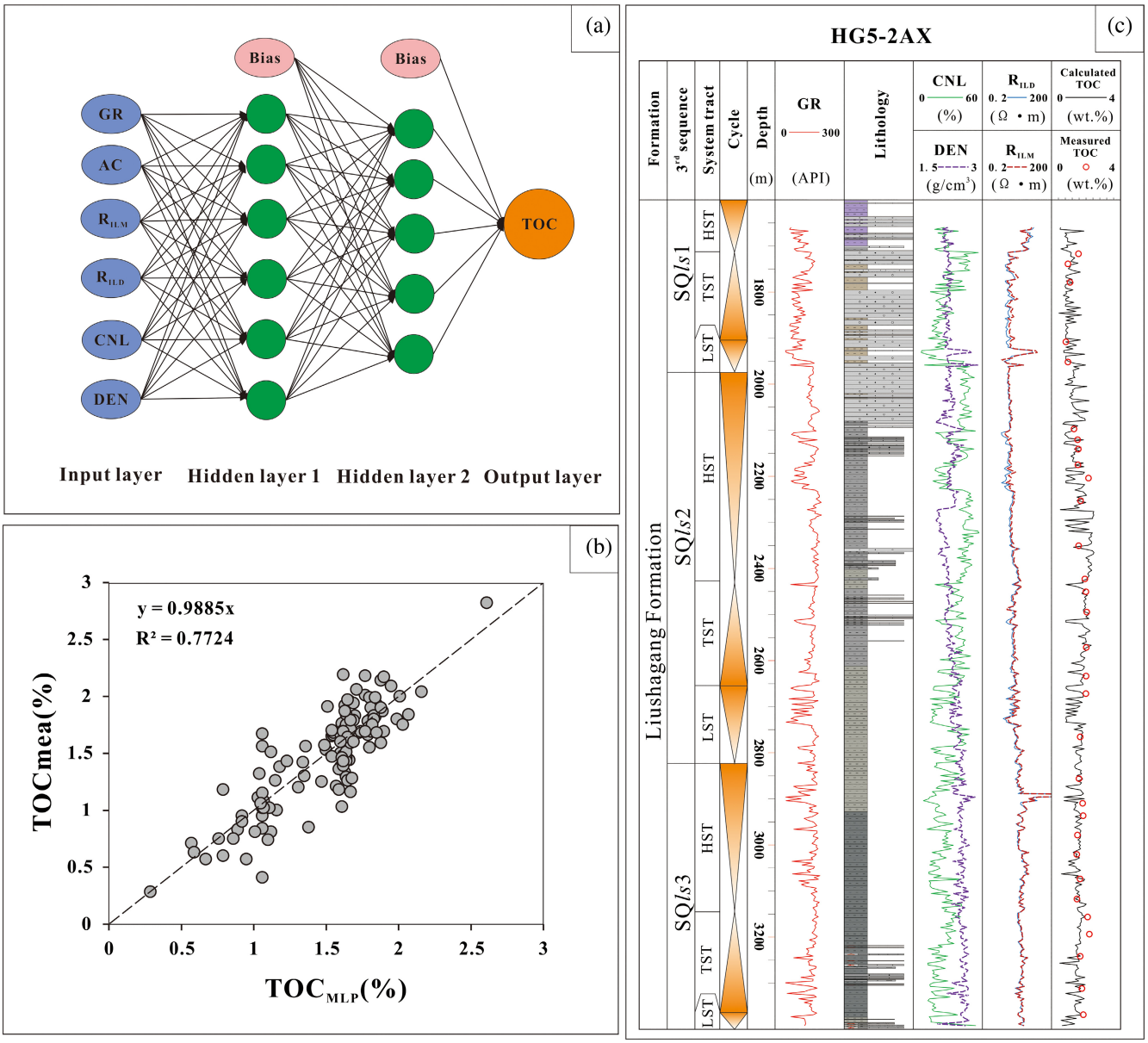

FIGURE 7 F (a) Diagram of the MLPNN algorithm structure; (b) prediction results of the MLPNN model; (c) the conventional logging curves and continuous TOC prediction curve of the well HG5-2AX

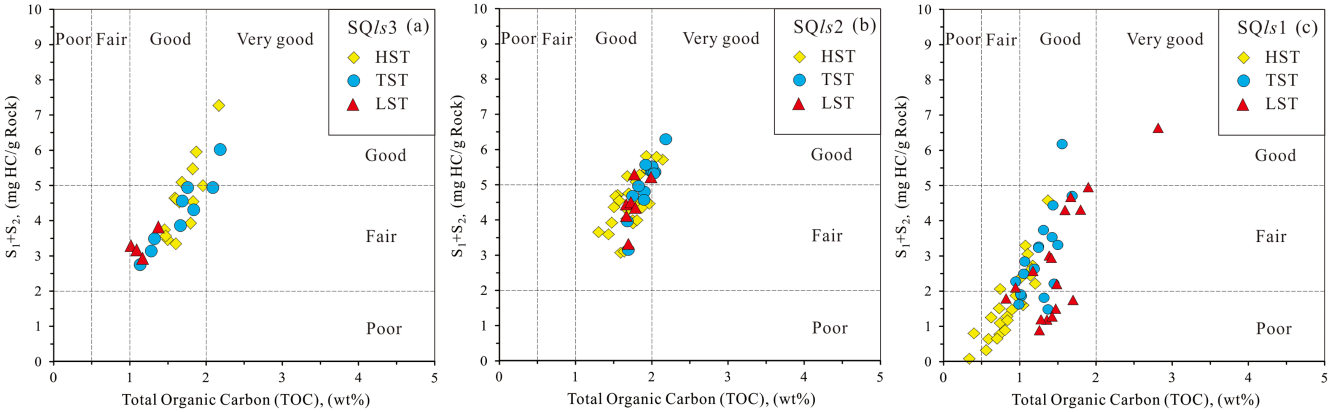

FIGURE 8 Cross-plot of GP versus TOC content of mudstones from SQls3 (a), SQls2 (b), and SQls1 (c) of the Liushagang Formation

method for TOC estimation, but it is not applicable to mudstone interlayers, due to the rapidly changing lithology and the difficulty in determining a baseline (Zeng et al., 2021). In this study, a multilayer perceptron neural network (MLPNN) method was chosen to build the TOC prediction model for the source rocks, because the mudstone interlayers are generally occurring in the delta front and turbidite fan facies in the western region of the Fushan Depression (Figure 4). MLPNN consists of an input layer, two hidden layers, and an output layer, and its algorithm structure is shown in Figure 7a. The process of the MLPNN is as follows: (a) randomly assign weights to the hidden layer neurons; (b) adjust the weights according to the back-propagation error; and (c) complete the training until the expected output is obtained. The correlation coefficient (R^2) between the measured TOC and estimated TOC is 0.7724 (Figure 7b). Figure 7c shows the prediction result of the Well HG5-2AX, and the TOC prediction curves of each individual wells in the western region of the Fushan Depression were obtained by this model.

5.2 | Source rock assessment within the sequence stratigraphic framework

5.2.1 | Organic matter richness

In this study, the cross-plot of GP versus TOC was used to evaluate the abundance of organic matter (Peters, 1986). The SQls3 mudstones are generally fair to good source rocks with the GP values and TOC values ranging from 2.75 to 7.27 mg/g and 1.01 to 2.19%, respectively, whereas good source rocks mainly occur in the ETST and HST (Figure 8a). The SQls2 mudstones are classified as fair to very good source rocks, with the GP values higher than 3.15 mg/g and the TOC values higher than 1.30% (Figure 8b). The mudstones from the LST (poor to very good source rocks, 0.83% < TOC < 2.82%, 0.89 mg/g < GP < 6.63 mg/g) and TST (poor to good source rocks, 0.95% < TOC < 1.7%, 1.48 mg/g < GP < 6.17 mg/g) of SQls1 have higher abundance of organic matter than that of the HST (poor to fair source rocks, 0.35% < TOC < 1.38%, 0.02 mg/g < GP < 4.57 mg/g) (Figure 8c). Note that most samples are classified as good source rocks based on TOC content, while they fall in the range of 'poor to fair source rock' according to the hydrocarbon generation potential, which mainly depends on the type of kerogen.

The significant variation of hydrocarbon generation potential of the mudstones from different system tracts may indicate that the quality of source rocks is controlled by the lake level. Those mudstones with TOC content lower than 1.0% were mainly occurred in SQls1-HST (Figure 8), corresponding to the lowest lake level (Figure 4). In contrast, other mudstones were deposited in a middle to high lake level environment (Figure 4). Therefore, we reasonably conclude that the rapid fall of lake level results in a large amount of deltaic or fan deltaic sediments deposition, causing the decrease of the organic richness. Moreover, it is noted that some mudstone samples from SQls1-LST–EST with higher TOC content

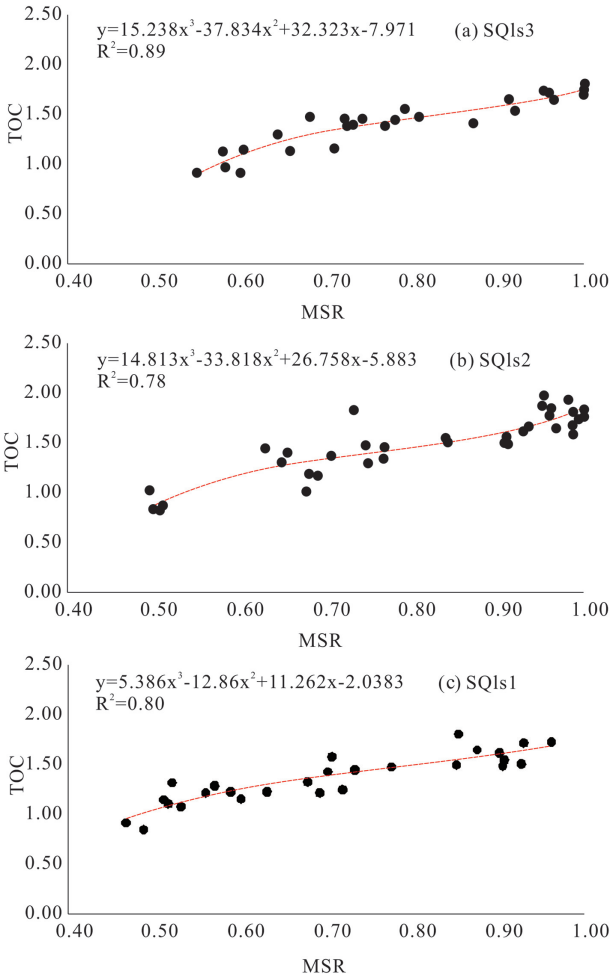

FIGURE 9 The correlation between TOC and MSR. MSR, the mudstone to stratum thickness ratio; R^2, correlation coefficient

(>1%) and lower GP (<2 mg/g) correspond to higher T_{max} and deeper burial depth (>3,400 m) (Table 1), indicating that they have a higher thermal maturity, resulting in poor present-day hydrocarbon generation potential.

Determining the mean TOC areal distribution of mudstones is of great significance for source rock assessment. The steps of the prediction for the spatial distribution of TOC content are as follows: (a) employ the MLPNN model to obtain the TOC prediction curves in individual wells; (b) count the mean TOC values of mudstones of different sequences in each well; (c) establish the correlation between TOC and depositional facies (mudstone to stratum thickness ratios) (Figure 9) (Lai, Li, Liu, Mao, Wang, et al., 2020; Ogiesoba & Hammes, 2014); (d) correction by the measured TOC data; and (e) obtain the distribution of the TOC content within the sequence stratigraphic framework. The estimation equations are as follows:

$$\mathrm{SQls3}: \mathrm{TOC} = 15.238 \times (\mathrm{MSR})^3 - 37.834 \times (\mathrm{MSR})^2 + 32.323 \times (\mathrm{MSR}) - 7.971$$

$$R^2 = 0.89 \quad (1)$$

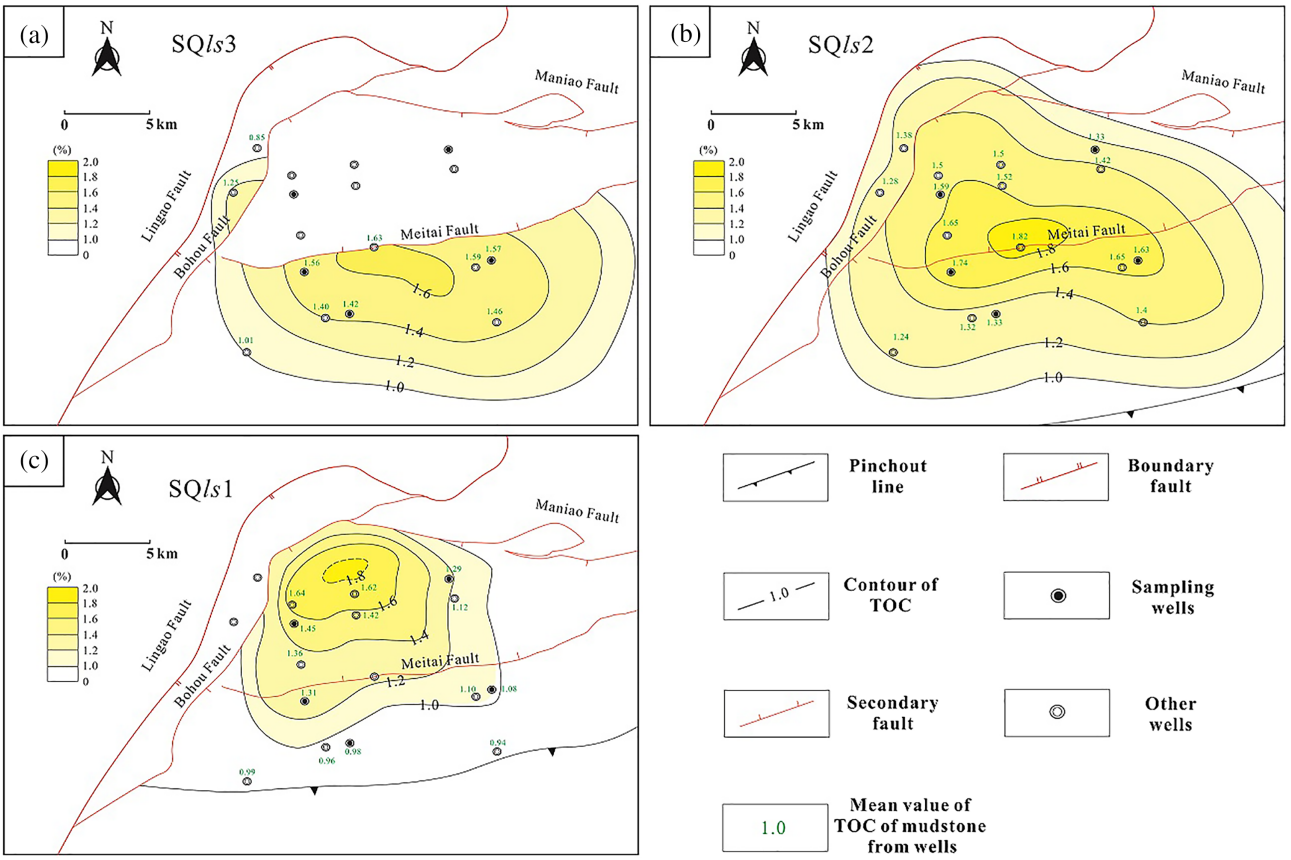

FIGURE 10 Contour maps of the average TOC content of the mudstones in SQls3 (a), SQls2 (b), and SQls1 (c)

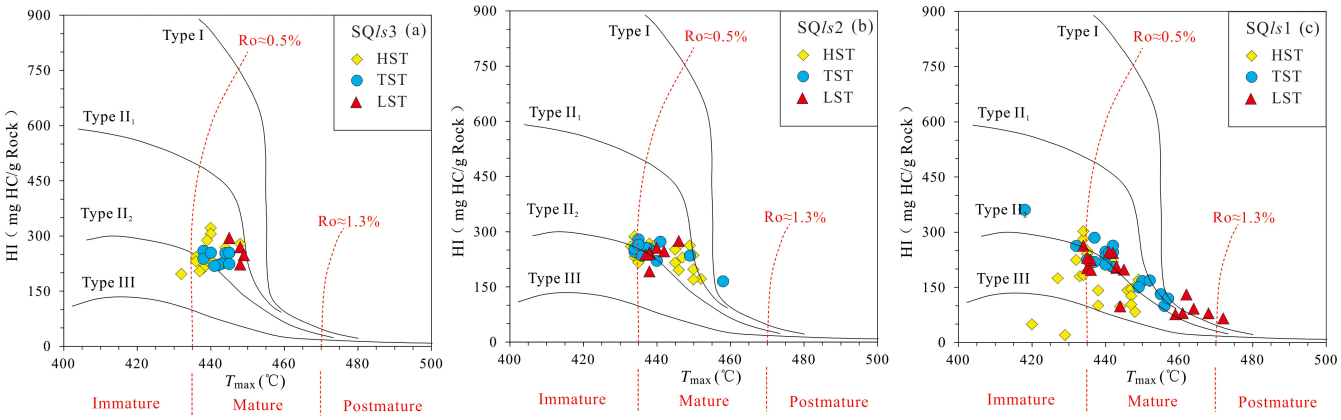

FIGURE 11 Cross-plot of HI versus T_{max} of mudstones from SQls3 (a), SQls2 (b), and SQls1 (c) of the Liushagang Formation

$$\mathrm{SQls2:TOC} = 14.813 \times (\mathrm{MSR})^3 - 33.818 \times (\mathrm{MSR})^2 + 26.758 \times (\mathrm{MSR}) - 5.883$$

$$R^2 = 0.78 \quad (2)$$

$$\mathrm{SQls1:TOC} = 5.386 \times (\mathrm{MSR})^3 - 12.86 \times (\mathrm{MSR})^2 + 11.262 \times (\mathrm{MSR}) - 2.0383$$

$$R^2 = 0.80, \quad (3)$$

where TOC represents the total organic carbon content (wt%); MSR represents the mudstone to stratum thickness ratio; R^2 represents the correlation coefficient.

The contour maps of mean TOC content of source rocks of the Liushagang sequences are given in Figure 8. The mean TOC values of SQls3 mudstones ranges from 1.0 to 1.6%, indicating that the source rocks in the most areas of the southern slope meet the criterion of

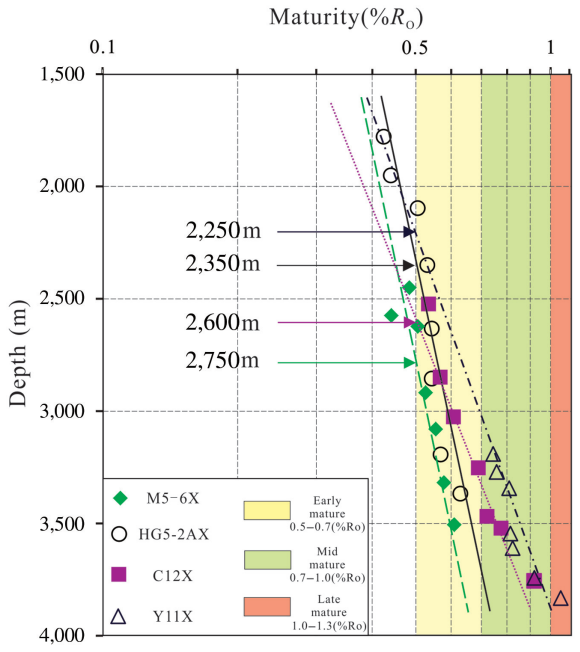

FIGURE 12 Fitting between vitrinite reflectance (*Ro*) and corresponding depth of representative wells

good source rocks (Figure 10a). During the SQls2 period, the rising lake level led to the expansion of the distribution range of good source rocks (1.0% < TOC < 1.8%). The areas with higher abundance of organic matter migrated from the southern slope to the centre of Huangtong Sag (Figure 10b). The lake shrank northward during the SQls1 period, and good source rocks (1.0% < TOC < 1.8%) mainly distributed in the north of Huangtong Sag (Figure 10c). In summary, the areas with higher organic matter abundance and mudstone depocenters migrate northward during the Liushagang period.

5.2.2 | Kerogen types of organic matter

Apart from the abundance of organic matter, the kerogen type is another key parameter, which distinguishes oil-prone and gas-prone source rocks (Hunt, 1979). Cross-plots of hydrogen index (HI=S_2/TOC, mg HC/g TOC) versus T_{max} were used to distinguish the kerogen type of source rock samples (Bordenave, Espitalié, Leplat, Oudin, & Vandenbrouke, 1993; Peters, 1986). Figure 11a,b indicate that the mudstones from SQls3 and SQls2 are dominated by Type II_1 to Type II_2 kerogen with higher HI values. The kerogen type of SQls1 is mainly Type II_2, with minor Type III kerogen depositing in the HST

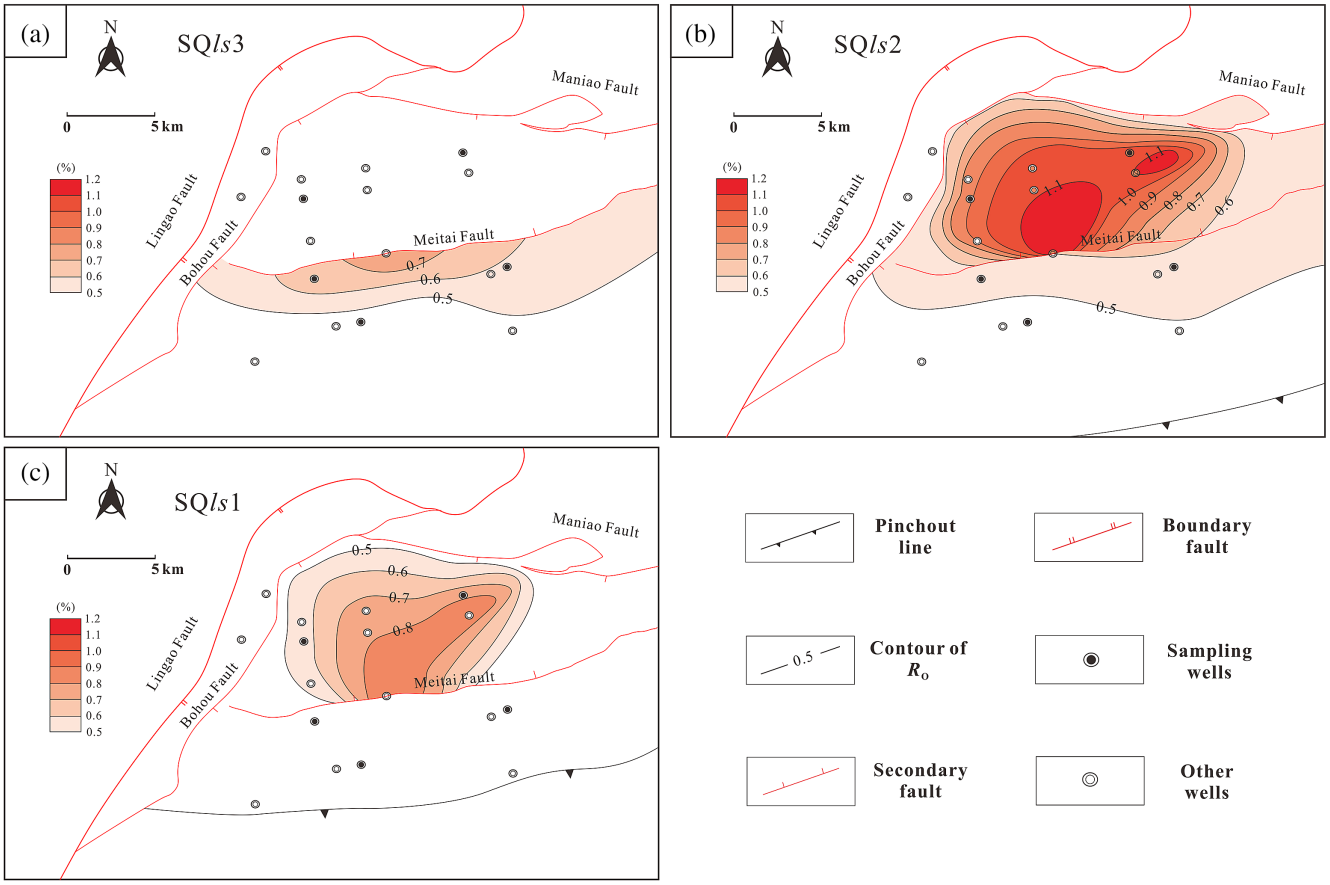

FIGURE 13 Contour maps of vitrinite reflectance (*Ro*) values of SQls3 (a), SQls2 (b), and SQls1 (c)

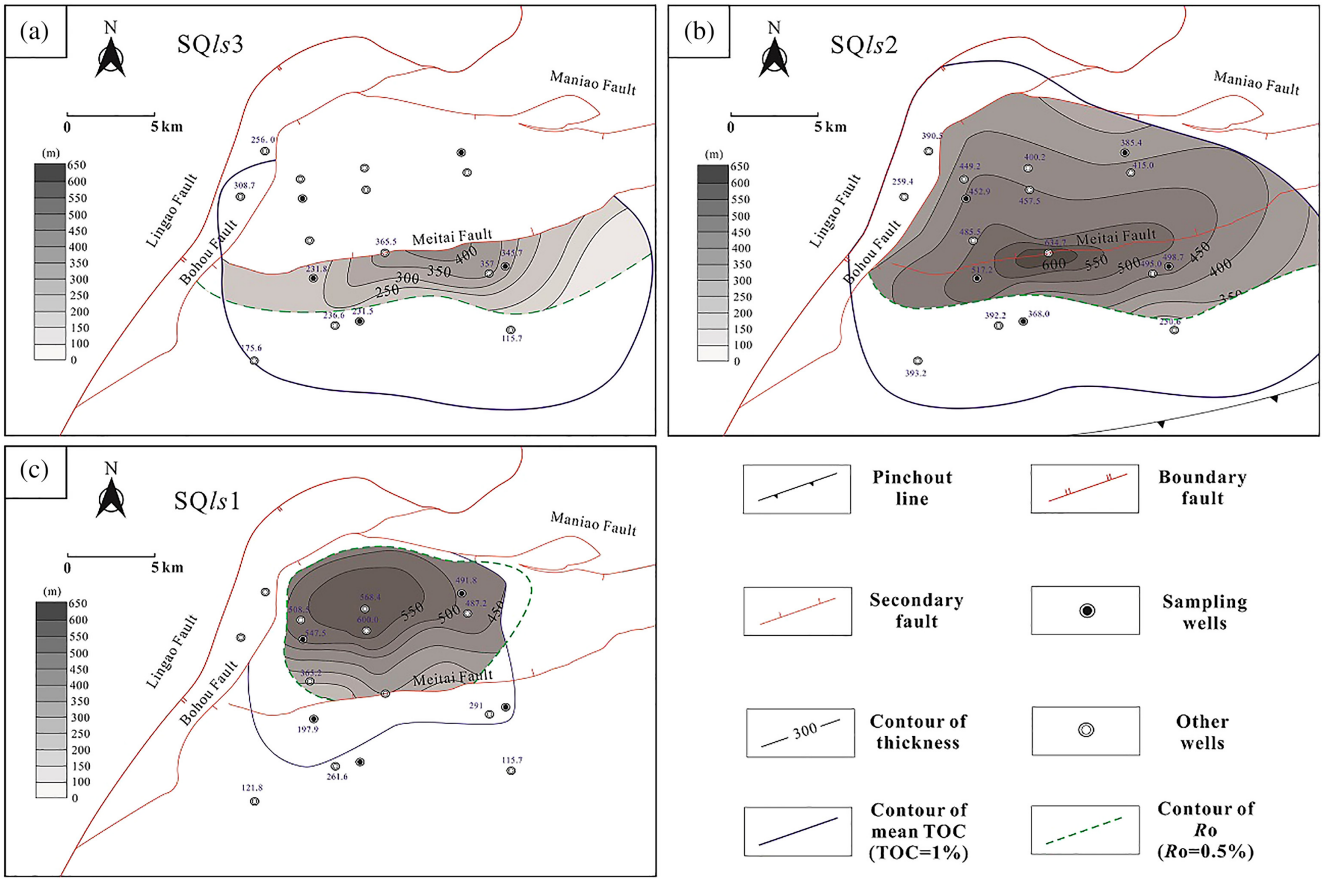

FIGURE 14 Distribution of the effective source rock kitchens of SQls3 (a), SQls2 (b), and SQls1 (c)

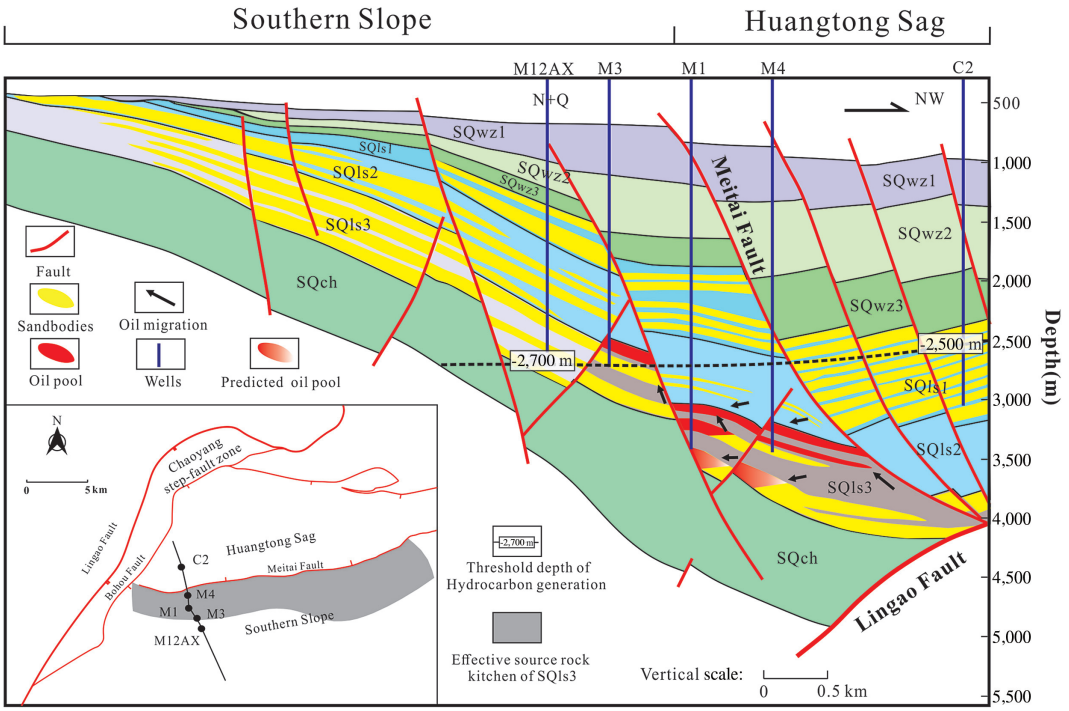

FIGURE 15 Petroleum migration and accumulation model of southern slope in the west region of the Fushan Depression

(Figure 11c). In conclusion, the organic matter types of the mudstones of the Liushagang Formation are mainly dominated by mixed kerogen with medium oil-prone ability.

5.2.3 | Thermal maturity of organic matter

T_{max} and *Ro* are commonly used parameters indicating the thermal evolutionary levels of source rocks. In this study, the T_{max} and Ro values of source rock samples range from 418 to 472°C and 0.42 to 1.05%, respectively, suggesting that their maturity is mainly in the early mature to mid mature stage (Figures 11 and 12). However, regional thermal maturity cannot be studied through the limited number of T_{max} and *Ro* data. Four representative wells (ie., M5-6X, HG5-2AX, C12X, Y11X) from different structural units, distributed in the south-west, south-east, north-west, and north-east of the study area, respectively, were chosen to establish the correlation between *Ro* and depth (Figure 10). The present-day burial depths correspond to the threshold of hydrocarbon generation in well M5-6X, HG5-2AX, C12X, and Y11X were estimated as 2,750, 2,250, 2,600, and 2,350 m, respectively.

Contour maps of *Ro* values of the Liushagang sequences were obtained by fitting equations and average burial depths (Figure 13). The SQls3 mudstones are classified as immature to early mature source rocks, and distribute in a limited area of the southern slope, with the *Ro* values ranging from 0.5 to 0.7% (Figure 13a). The mudstones from SQls2 have reached the highest maturity stage of source rocks in the Liushagang Formation, with the highest *Ro* value of 1.1%. All the source rocks from the Huangtong Sag reached the mid mature to late mature stage (Figure 13b). The maturity of SQls1 mudstones is lower than that of SQls2, with the *Ro* values ranging from 0.5 to 0.8% (Figure 13c).

M. Li et al. (2007) rebuilt the burial and thermal histories of the Fushan Depression by numerical modelling and indicated that the oil accumulating of the Palaeogene petroleum system occurred in Late Miocene (10–6 Ma). Based on the comprehensive analysis of the burial and thermal histories, we can reasonably conclude that the maturity of the Liushagang source beds during 10–6 Ma is slightly lower than the current maturity.

5.3 | Prediction of the effective source rock kitchen and controlling factors

Thick, organic-rich potential source rocks can become effective source rocks after sufficient burial and thermal maturation (Peters, Magoon, Valin, & Lillis, 2007). Because of the similar kerogen type, comparison of thickness, organic richness, and maturity information for source rocks was used to determine the effective source rock. In this study, the criterion of effective source rock is defined as good to very good source rocks (TOC > 1%) with higher hydrocarbon potential and thermal maturity in the mature range (Ro > 0.5%).

Based on comprehensive analysis of areal mudstone thickness, TOC content, and thermal maturity, the distribution of effective source rock kitchens of the Liushagang sequences was shown in Figure 14. As a result, the strip-shaped area of the southern slope with about 3 km wide of SQls3 (200–400 m thickness), the whole Huangtong Sag of SQls2 (350–600 m thickness), and the central and northern part of Huangtong Sag of SQls1 (400-550 m thickness) were identified as the effective source rock kitchen ranges (Figure 12). In general, thick organic-rich mudstones widely occurred in all the Liushagang sequences. It can be inferred that the areal thermal maturity of source rocks controls the distribution of effective source rock kitchens.

5.4 | Implication for hydrocarbon exploration

Petroleum accumulations are more likely to originate from the active source rocks in the same geographic location (Magoon, 2004). In other words, determining the ranges of effective source rock kitchen plays a vital role in the selection of exploration targets.

Prospectors focused on the southern slope zone due to the occurrence of a large number of sandstone reservoirs, but only SQls3 oil pools have been discovered, and fewer accumulations have been found in the south of Well M3 (Figure 15). Based on oil-source correlation, previous studies pointed out that the crude oil in the southern slope is mainly derived from the local SQls3 source rocks, rather than the SQls2 and SQls1 mudstones from the Huangtong Sag (Lu et al., 2016; Shi, Guo, Liao, Cheng, & Li, 2020). However, the relatively deeper hydrocarbon generation threshold depth results in the limited occurrence of effective source rocks of SQls3 (Figure 14). Therefore, it can be inferred that the small amounts of effective source rocks are the reason for the fewer hydrocarbon accumulations on the southern slope of the western region of the Fushan Depression. The sand bodies of lower parts of SQls3 within the range of the effective source kitchen are better exploration targets than their southern counterparts, due to their sufficient hydrocarbon source.

6 | CONCLUSIONS

In this study, a comprehensive source rock evaluation was carried out by geochemical experiment analysis, combined with sequence stratigraphy theory and logging geochemical prediction. Four main conclusions can be drawn as follows:

1. Source rocks of SQls3, SQls2, and SQls1 with a thickness of 100-600 m are widely distributed in the western region of the Fushan Depression and are characterized by a distributional pattern thinning to the surroundings, and thicker to the north and thinner to the south, respectively. The lacustrine depositional centre migrated to the north Huangtong Sag during the Liushagang period.
2. Fair to very good source rocks dominated with Type II kerogen are occurred in the EST–HST of SQls3, SQls2, and LST–EST of SQls1, whereas the source beds in HST of SQls1 are characterized by

poor to fair hydrocarbon generation potential with Type III kerogen.

3. Thermal maturity is the main factor to control the distribution of effective source rock kitchens. The strip-shaped area of the southern slope with about 3 km wide, the whole Huangtong Sag and the central-northern Huangtong Sag were classified as the effective source rock kitchen ranges of SQls3, SQls2, and SQls1, respectively.
4. The determination of the effective source rock kitchen range has a guiding role for oil and gas exploration. Fewer hydrocarbon accumulations were found in the southern slope due to the deeper hydrocarbon generation threshold and the limited occurrence of effective source rock kitchens.

ACKNOWLEDGEMENTS

This study was funded by the Hainan Fushan Oilfield Exploration and Development Company (2020-HNYJ-003). The authors are grateful for Lei Zhu's assistance with the geochemical analysis.

CONFLICT OF INTEREST

The authors declare that they have no known competing financial interests or personal relationships that could have appeared to influence the work reported in this paper.

PEER REVIEW

The peer review history for this article is available at https://publons.com/publon/10.1002/gj.4419.

DATA AVAILABILITY STATEMENT

The data that supports the findings of this study are available in Table 1 of this article.

REFERENCES

Bordenave, M. L., Espitalié, J., Leplat, P., Oudin, J. L., & Vandenbrouke, M. (1993). Screening techniques for source rock evaluation. In M. L. Bordenave (Ed.), *Applied petroleum geochemistry* (pp. 218–278). Paris, France: Editions Technip.

Catuneanu, O. (2020). Sequence stratigraphy in the context of the 'modeling revolution'. *Marine and Petroleum Geology*, *116*, 104309.

Chen, S., Gan, H., Shi, Y., Zhao, Y., & Wang, X. (2015). Geochemical features and geologic significance of source rocks in Fushan Sag, Beibuwan Basin. *Petroleum Geology and Recovery Efficiency*, *22*(1), 14–25. (in Chinese with English abstract)

Feng, Z. (2004). Single factor analysis and multifactor comprehensive mapping method: Reconstruction of quantitative lithofacies palaeogeography. *Journal of Palaeogeography*, *6*, 3–19. (in Chinese with English abstract)

Fertl, W., & Chilingar, G. (1988). Total organic carbon content determined from well logs. *SPE Formation Evaluation*, *3*(02), 407–419.

Flint, S., Knight, S., & Tilbrook, A. (1998). Application of high-resolution sequence stratigraphy to northwest Hutton Field, northern North Sea: Implications for management of a mature Brent Group field. *AAPG Bulletin*, *82*, 1416–1436.

Gan, H., Wang, H., Shi, Y., Ma, Q., Liu, E., Yan, D., & Pan, Z. (2020). Geochemical characteristics and genetic origin of crude oil in the Fushansag, Beibuwan Basin, South China Sea. *Marine and Petroleum Geology*, *112*, 104114.

Gong, Z. S., Li, S. T., & Xie, T. (1997). *Continental margin basin analysis and hydrocarbon accumulation of the Northern South China Sea* (pp. 1–510). Beijing, China: Science Press.

He, C., Ji, L., Su, A., Wu, Y., Zhang, M., Zhou, S., … Ma, Y. (2019). Source-rock evaluation and depositional environment of black shales in the Triassic Yanchang Formation, southern Ordos Basin, north-central China. *Journal of Petroleum Science and Engineering*, *173*, 899–911.

Higgs, K. E., King, P. R., Raine, J. I., Sykes, R., Browen, G. H., Crouch, E. M., & Baur, J. R. (2012). Sequence stratigraphy and controls on reservoir sandstone distribution in an Eocene marginal marine-coastal plain fairway, Taranaki Basin, New Zealand. *Marine and Petroleum Geology*, *32*, 110–137.

Hunt, J. M. (1979). *Petroleum geochemistry and geology* (1st ed., pp. 743–750). New York, NY: Freeman.

Hunt, J. M. (1996). *Petroleum geochemistry and geology* (2nd ed., p. 743). New York, NY: W.H. Freeman and Company.

Jin, S., Wang, H., Cao, H., Gan, H., & Chen, S. (2020). Lake-type controls on sedimentary infill and petroleum source rocks in the Palaeogene Fushan Depression, Beibuwan Basin, South China. *Geological Journal*, *55*(5), 3936–3956.

Kieft, R. L., Jackson, A. L., Hampson, G. J., & Larsen, E. (2010). Sedimentology and sequence stratigraphy of the Hugin Formation, Quadrant 15, Norwegian sector, South Viking Graben. *Petroleum Geology Conference Proceedings*, *7*, 157–176.

Lai, H., Li, M., Liu, J., Mao, F., Liu, J., Xiao, H., … Shi, S. (2020). Source rock types, distribution and their hydrocarbon generative potential within the Paleogene Sokor-1 and LV formations in Termit Basin, Niger. *Energy Exploration & Exploitation*, *38*(6), 2143–2168.

Lai, H., Li, M., Liu, J., Mao, F., Wang, Z., Liu, W., & Yang, L. (2020). Source rock assessment within a sequence stratigraphic framework of the Yogou Formation in the Termit Basin, Niger. *Geological Journal*, *55*(4), 2473–2494.

Li, M., Lai, H., Mao, F., Liu, J., Xiao, H., & Tang, Y. (2018). Geochemical assessment of source rock within a stratigraphic geochemical framework: Taking Termit Basin (Niger) as an example. *Earth Science*, *43*(10), 3603–3615. (in Chinese with English abstract)

Li, M., Simoneit, B. R. T., Zhong, N., & Fang, R. (2013). The distribution and origin of dimethyldibenzothiophenes in sediment extracts from the Liaohe Basin, East China. *Organic Geochemistry*, *65*, 63–73.

Li, M., Wang, T., Liu, J., Lu, H., Wu, W., & Gao, L. (2008). Occurrence and origin of carbon dioxide in the Fushan Depression, Beibuwan Basin, South China Sea. *Marine and Petroleum Geology*, *25*, 500–513.

Li, M., Wang, T., Liu, J., Zhang, Z., Lu, H., Ma, Q., & Gao, L. (2007). A discussion on hydrocarbon accumulation dating determined by homogenization temperature and burial history of fluid inclusions-An examples from the Fushan Depression, Beibuwan Basin. Oil and Gas. *Geology*, *28*(2), 151–158. (in Chinese with English abstract)

Li, Y., Lin, S., Wang, H., & Luo, D. (2017). Depositional setting analysis using seismic sedimentology: Example from the Paleogene Lishagang sequence in the Fushan depression, South China Sea. *Geodesy and Geodynamics*, *8*, 347–355.

Liu, E., Wang, H., Feng, Y., Pan, S., Jing, Z., Ma, Q., … Zhao, J. (2020). Sedimentary architecture and provenance analysis of a sublacustrine fan system in a half-graben rift depression of the South China Sea. *Sedimentary Geology*, *409*, 105781.

Liu, E., Wang, H., Li, Y., Leonard, N., Feng, Y., Pan, S., & Xia, C. (2015). Relative role of accommodation zones in controlling stratal architectural variability and facies distribution: Insights from the Fushan Depression, South China Sea. *Marine and Petroleum Geology*, *68*, 219–239.

Liu, E., Wang, H., Li, Y., Zhou, W., Leonard, N., Lin, Z., & Ma, Q. (2014). Sedimentary characteristics and tectonic setting of sublacustrine fans in a half-graben rift depression, Beibuwan Basin, South China Sea. *Marine and Petroleum Geology*, *52*, 9–21.

Liu, E., Wang, H., Lin, Z., Li, Y., & Ma, Q. (2012). Characteristics and hydrocarbon enrichment rules of transfer zone in Fushan Sag, Beibuwan

Basin. *Journal of Central South University (Science and Technology)*, *43*(10), 3946–3953. (in Chinese with English abstract)

Lu, Z., Gan, H., Shi, Y., Chen, S., Wang, H., & Ma, Q. (2016). Geochemical Characteristics of Crude Oil and Oil-Source Correlation in the Western Fushan Depression. *Earth Science*, *41*(11), 111–122. (in Chinese with English abstract)

Ma, Q., Zhao, S., Liao, Y., & Lin, Z. (2012). Sequence architectures of Paleogene Liushagang Formation and its significance in Fushan Sag of the Beibuwan Basin. *Earth Science - Journal of China University of Geosciences*, *37*(4), 667–678. (in Chinese with English abstract)

Magoon, L. B. (2004). Petroleum system: Nature's distribution system for oil and gas. *Encyclopedia of energy*, *4*, 823–836. https://doi.org/10.1016/b0-12-176480-x/00251-5.

Magoon, L. B., & Dow, W. G. (1994). The petroleum system. In L. B. Magoon & W. G. Dow (Eds.), *The petroleum system—From source to trap*. *AAPG Memoir* (Vol. 60, pp. 3–24). Tulsa, OK, USA: American Association of Petroleum Geologists.

Mancini, E. A., Obid, J., Badai, M., Liu, K., & Parcell, W. C. (2008). Sequence-stratigraphic analysis of Jurassic and Cretaceous strata and petroleum exploration in the central and eastern Gulf coastal plain, United States. *AAPG Bulletin*, *92*, 1655–1686.

Ogiesoba, O., & Hammes, U. (2014). Seismic-attribute identification of brittle and TOC-rich zones within the Eagle Ford Shale, Dimmit County, South Texas. *Journal of Petroleum Exploration and Production Technology*, *4*, 133–151.

Passey, Q., Creaney, S., Kulla, J., Moretti, F., & Stroud, J. (1990). A practical model for organic richness from porosity and resistivity logs. *AAPG Bulletin*, *74*, 1777–1794.

Peters, K. E. (1986). Guidelines for evaluating petroleum source rock using programmed pyrolysis. *AAPG Bulletin*, *70*, 318–329.

Peters, K. E., & Cassa, M. R. (1994). Applied source rock geochemistry. In L. B. Magoon & W. G. Dow (Eds.), *The petroleum system-From source to trap*. *AAPG Memoir* (Vol. 60, 93–115). Tulsa, OK, USA: American Association of Petroleum Geologists.

Peters, K. E., Magoon, L. B., Valin, Z. C., & Lillis, P. G. (2007). Source-rock geochemistry of the San Joaquin Basin Province, California. In H. Scheirer (Eds.), *Petroleum systems and geologic assessment of oil and gas in the San Joaquin Basin Province, California*: chap. 11. California, USA: U.S. Geological Survey.

Peters, K. E., Snedden, J. W., Sulaeman, A., Sarg, J. F., & Enrico, R. J. (2000). A new geochemical-sequence stratigraphic model for the Mahakam Delta and Makassar slope, Kalimantan, Indonesia. *AAPG Bulletin*, *84*(1), 12–44.

Rospondek, M. J., Szczerba, M., Malek, K., Góra, M., & Marynowski, L. (2008). Comparison of phenyldibenzothiophene distributions predicted from molecular modelling with relevant experimental and geological data. *Organic Geochemistry*, *39*, 1800–1815.

Schmoker, J. (1979). Determination of organic content of Appalachian Devonian shales from formation-density logs. *AAPG Bulletin*, *63*(9), 1504–1509.

Sheikh, H. E., Faris, M., Shaker, F., & Kumral, M. (2016). Mineralogy and source rock evaluation of the marine Oligo-Miocene sediments in some wells in the Nile Delta and North Sinai, Egypt. *Journal of African Earth Sciences*, *118*, 163–173.

Shi, Y., Guo, H., Liao, F., Cheng, G., & Li, X. (2020). Physical properties and geochemical characteristics of crude oil in Fushan Sag, Beibuwan Basin. *China Offshore Oil and Gas*, *32*(6), 31–42. (in Chinese with English abstract)

Souza, A. C. B. D., Nascimento, D. R. D., Filho, F. N., Batezelli, A., Santos, F. H. D., Oliveira, K. M. L., & Almeida, N. M. D. (2021). Sequence stratigraphy and organic geochemistry: An integrated approach to understand the anoxic events and paleoenvironmental evolution of the Ceará basin, Brazilian Equatorial margin. *Marine and Petroleum Geology*, *129*, 105074.

Tissot, B. P., & Welte, D. H. (1984). *Petroleum formation and occurrence* (Second Revised and Enlarged Edition) (pp. 495–546). Berlin, Germany: Springer-Verlag.

Xiao, H., Wang, T., Li, M., Lai, H., Liu, J., Mao, F., & Tang, Y. (2019). Geochemical characteristics of Cretaceous Yogou Formation source rocks and oil-source correlation within a sequence stratigraphic framework in the Termit Basin, Niger. *Journal of Petroleum Science and Engineering*, *172*, 360–372.

Xie, C., Hu, M., Jia, X., & Hu, Z. (2011). Sedimentary facies and its evolution of the Lower Member of Paleogene Xingouzui Formation in Mawangmiao area of Jianghan Basin. *Journal of Paleogeography*, *13*, 209–220. (in Chinese with English abstract)

Zeng, B., Li, M., Zhu, J., Wang, X., Shi, Y., Zhu, Z., … Wang, F. (2021). Selective methods of TOC content estimation for organic-rich interbedded mudstone source rocks. *Journal of Natural Gas Science and Engineering*, *93*(5), 104064.

How to cite this article: Zeng, B., Li, M., Wang, X., Wang, F., Gong, C., Lai, J., & Shi, Y. (2022). Source rock evaluation within a sequence stratigraphic framework of the Palaeogene Liushagang Formation in the Fushan Depression, South China Sea. *Geological Journal*, *57*(6), 2409–2427. https://doi.org/10.1002/gj.4419